actuators

MDPI

Article

High-Bandwidth Active Impedance Control of the Proprioceptive Actuator Design in Dynamic Compliant Robotics

Simon Hjorth Jessing Lund, Peter Billeschou and Leon Bonde Larsen *

Advanced Computer Systems Group, University of Southern Denmark, Campusvej 55, 5230 Odense, Denmark; simonjessing@gmail.com (S.H.J.L.); pebil@mmmi.sdu.dk (P.B.)

* Correspondence: lelar@mmmi.sdu.dk; Tel.: +45-66-15-76-97

Received: 8 September 2019; Accepted: 9 October 2019; Published: 17 October 2019

Abstract: Dynamic compliant robotics is a fast growing field because of its ability to widen the scope of robotics. The reason for this is that compliant mechanisms may ensure safe/compliant interactions between a robot and an external element—for instance, a human operator. Active impedance control may widen the scope even further in relation to passive elements, but it requires high-bandwidth robust torque and active impedance control which induces high-noise issues even if high-end sensors are used. To address these issues, a complete controller design scheme, including Field-Oriented Control (FOC) of a Brushless Direct Current (BLDC) motor, is proposed. In this paper, controller designs for controlling the virtual impedance, motor torque and field are proposed which enables high-bandwidth robust control. Additionally, a novel speed and angle observer is proposed that aims to reduce noise arising in the angle sensor (typically a 12-bit magnetic encoder) and a Kalman/Luenberger based torque observer is proposed that aims to reduce noise arising in the phase current sensors. Through experimental tests, the combination of the controller designs and observers facilitated a closed-loop torque bandwidth of 2.6 kHz and a noise reduction of 13.5 dB (in relation to no observers), at a sample rate and Pulse Width Modulation (PWM) frequency of 25 kHz. Additionally, experiments verified a precise and high performing controller scheme both during impacts and at a variety of different virtual compliance characteristics.

Keywords: proprioceptive control; virtual compliance; field oriented control; high noise attenuation; legged robots; motor control; observer; Kalman filter; torque control; high bandwidth; BLDC

1. Introduction

Compliance enables robotics to be used in contexts that include transitions of energy between a robot and fragile or unknown external elements—for instance, interactions with humans or walking on rugged terrain. This ability widens the scope of robotics which makes compliant robotics a fast advancing field. For this reason, the advancements in compliant robotics has made its footprint in areas where compliant interactions are required—for instance, legged robotics [1], rehabilitation robotics [2], wearable robotics [3], robotics surgery [4], robotic prostheses [5], soft robotics [6], collaborative robotics [7] and active vehicle suspension [8].

1.1. Compliant Actuators

In order to facilitate compliance in a robot, it must include a compliant actuator. Five of the most commonly used electromagnetic actuator designs for compliant actuation of robots [9] are illustrated in Figure 1.

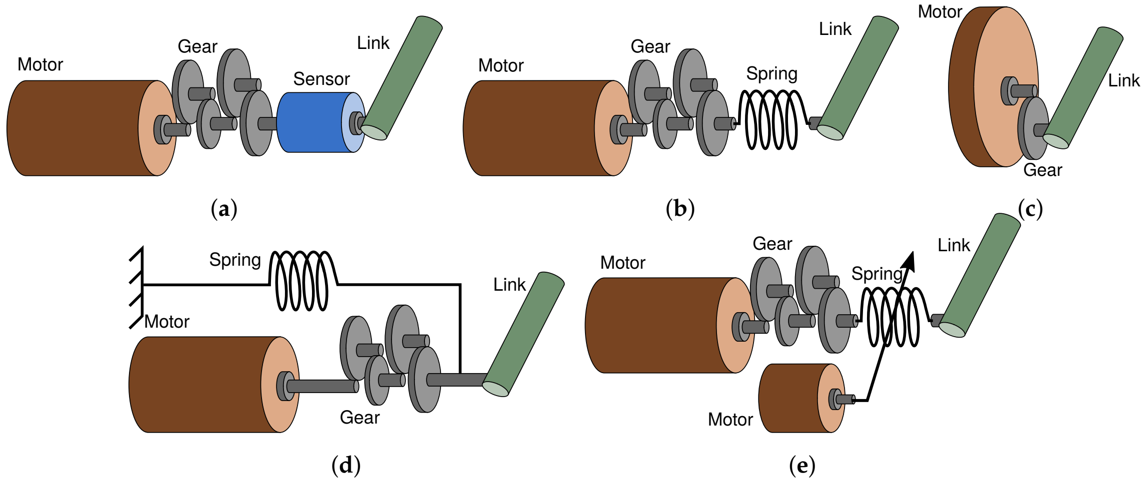

Figure 1. Illustration of five compliant actuators. The figures are replicated from the three corresponding figures in [1]. The sample delay listed below refers to the delay, between an occurring impact to an opposing force that has been applied, introduced using a digital impedance controller.

(a) **Geared Motor with Force/Torque sensor (GMS)** embeds a low-diameter motor and a high gear ratio transmission to actuate the robot link. A torque or force sensor is used as feedback to perform torque or force control. Pros:variable impedance response, high torque density. Cons: sample delay (cannot mitigate high speed shocks), low open-loop force controller bandwidth (at end-effector), low Z-width [10], low force transparency.

(b) **Series Elastic Actuator (SEA)** includes a low-diameter motor and a high gear ratio transmission to actuate the robot link. A spring is connected between the gears and the end-effector of the robot link. Pros: high torque density, high energy efficiency, simple control, no sample delay* (can mitigate high speed shocks). Cons: fixed impedance response [9], it offers improved force transparency and open-loop force controller bandwidth (at end-effector) in relation to GMS and PEA [11], but is not comparable to the proprioceptive actuator design on this matter [1,9,12,13].

(c) **Proprioceptive actuator** includes a high-diameter motor and a low gear ratio transmission to actuate the robot link. As the transparency between the motor shaft and the end-effector is very low (due to low gearing and high stiffness), the motor phase currents can be used to estimate the torque at the end-effector (proprioception). Pros: high open-loop force controller bandwidth (at end-effector), high force transparency [1,9,12,13], high Z-width [10]. Cons: complex control, sample delay* (cannot mitigate high speed shocks), lower energy efficiency and torque density than other electromagnetic actuators [1].

(d) **Parallel Elastic Actuator (PEA)** includes a low-diameter motor and a high gear ratio transmission to actuate the robot link. Additionally, it includes a spring which is connected in parallel with the robot link. Pros: high torque density, high efficiency [14], simple control, no sample delay* (can mitigate high speed shocks). Cons: fixed impedance response, low open-loop force controller bandwidth (at end-effector), low force transparency.

(e) **Variable Stiffness Actuator (VSA)** is typically comprised of the same elements as SEA, where an additional motor is controlling the stiffness of the elastic element. Pros: high torque density, high energy efficiency [14], variable impedance response, no sample delay* (can mitigate high speed shocks). Cons: complex control, low open-loop force controller bandwidth (at end-effector), low force transparency.

Conventionally, compliant robots are equipped with passive springs and dampers (e.g., SEA and PEA) which enable a smooth transition of energy between the robot and an external element without damaging either and ensuring stable operation. However, the dynamic response is restricted to those enabled by the selected passive elements which limits the dynamic response and thereby the variety of achievable interactions. It is often required to adapt the impedance (in order to retain stable operation) which can be done by deploying the VSA or an active impedance controller (often referred to as virtual compliance) [10,15,16] which is obtainable using GMS or the proprioceptive actuator.

The high gear ratios used in GMS, SEA, PEA and VSA enable high torque. However, as the transmission path from the motor shaft to the end-effector of GMS, SEA, PEA and VSA includes many components (gears, sensors, springs, etc.) that introduce elasticity and inertia, the force transparency is relatively low [1,9,12,13]. Hence, these four actuators are not able to accomplish high-bandwidth open-loop force control of the end-effector which is required in order to perform dynamic physical interactions. As the proprioceptive actuator only includes a low ratio gearing and no other mechanical components are required, it is capable of achieving a much higher open-loop force controller bandwidth of the end-effector which enables dynamic physical interactions [1]. In fact, studies show that the dynamic range of achievable virtual impedances (Z-width) mainly depends on the closed-loop torque bandwidth [10]. Using the proprioceptive actuator design, lower gear-ratio can be compensated for by using a high-diameter motor.

In order to enable a wide Z-width, MIT initially designed their Mini Cheetah robot with a closed-loop torque bandwidth of 4.5 kHz [12] by using the proprioceptive actuator design. However, due to the high bandwidth, high audible noise was observed by the author of [12]. This is expected since active impedance control typically involves computing a torque reference based on the error between desired and actual speed and position. As speed needs to be computed at high rates (typically 5 kHz to 50 kHz) from the angular position which is typically measured by a magnetic encoder (typically around 12-bit resolution), noise will be injected into the torque loop. A high closed-loop torque controller bandwidth induces minimal filtering effect in the torque controller meaning that the noise arising from computing the derivative of the angle gets directly injected into the phase voltages and will appear as audible noise in the motor. Additionally, the noise from the encoder and the phase current sensors are being injected into the phase voltages when using Field Oriented Control (FOC) as it is used in the computation of the torque and field components [17].

1.2. Existing Impedance Control Systems

When a robot is deployed in an environment with unknown stiffness and interaction tasks are required (such as human-robot interactions), problems of instability or high force-overshoot may occur which can potentially create a dangerous situation. To solve that issue, a method based on the energy tank theory was proposed in [18] with the purpose of preserving the passivity of the controlled system. To reduce instabilities and force overshoot, [19] uses optimal control by employing a Linear-Quadratic Regulator (LQR) to adapt the controller gains. In addition, an Extended Kalman Filter (EKF) was used to estimate the stiffness of the environment while online.

The concept of collaborative robots (often referred to as cobots) was invented back in 1999 partly to assist people in heavy duty tasks. However, until 2009, the only heavy duty human-assisting tools deployed in the industry were weight compensators/balancers which were not sufficient to avoid back injuries. Therefore, more advanced solutions were needed. Reference [20] proposed a framework that allows for a direct human-machine collaboration (with no minimum security distance) where the robot alternates between active and passive collaboration during assembly with the purpose of unburdening the worker. Reference [21] proposed a manual guidance system that allows for human guidance (by direct contact) of a cobot which acts as an active weight compensator.

In order to increase flexibility of industrial robots, they are often deployed on a mobile base. This adds elasticity to the robot base which affects the dynamics of the interaction between the robot and the environment. Reference [22] proposed an interaction controller that is able to adapt its parameters online to compensate for robot base elasticity.

1.3. Work Contribution

This paper analyzes how the motor is affected by noise arising from the angle sensor and the three phase current sensors. Based on the results quantified by this analysis, a novel angle and speed observer is proposed. Previously proposed observers are mostly used for high-speed sensorless control [23–25] rather than for reducing the noise (or increasing the resolution) of a deployed angle sensor at variable speed with minimal phase lag which is needed in dynamic compliant robotics. The proposed angle and speed observer enables filtering as well as precise estimation of mechanical angle, electrical angle and speed for variable speed, high-bandwidth and high-torque control. Additionally, it features minimal phase delay and is intended for FOC commutation of BLDC motors.

Most papers published within the area of active impedance control of compliant robotics (using the proprioceptive actuator design) deal with abstract issues such as the robotics control and mechanical design rather than how to properly design the two main required loops (the torque and impedance loop) for achieving high-bandwidth active impedance control. Therefore, model-based controller design methodologies are proposed which enable high-bandwidth and robust control.

The main contribution of this work is the proposal of a complete and reproducible controller design scheme which facilitates a combination of high-bandwidth (or high Z-width), high-precision and low-noise active impedance control. This mainly consists of the following three parts:

1. The torque and field controller design (Section 3.1) describes a "best practice" tuning of the torque and field controller parameters for high-bandwidth and highly stable closed-loop torque control of Brushless Direct Current (BLDC) motors tailored for active impedance controlled compliant robotics.
2. The active impedance controller design (Section 3.2) describes novel equations to derive controller gains that ensure a virtual compliance response closely related to the response of its physical counterpart (a mass-spring-damper system).
3. The observer designs (Sections 6 and 7) describe two observers that enable high-bandwidth low-noise motor control. In particular, Section 6 describes a novel observer that is tailored for robust high-bandwidth, low-noise compliant robotics to achieve noise-reduced angle and speed estimations as compared to using the raw angle and speed obtained from the encoder directly.

The novelty of parts 1 and 2 is not significant alone, but they are important parts of achieving the combination high-bandwidth (or high Z-width), high-precision, low-noise active impedance control and are therefore—as a union (including all three parts)—considered novel. Parts 1 and 2 stand in contrast to most papers within active impedance controlled robotics that tend to neglect the low-level control design or use sub-optimal solutions. In addition, in contrast to most papers within high bandwidth active impedance control, this work deals with the problem of noise (arising due to the combination of high bandwidth torque and active impedance control) with the introduction of the novel speed and angle observer. Applying this observer, a high torque bandwidth (comparable to that in MIT's Mini Cheetah) with low noise issues is obtainable.

Additionally, a novel and reproducible test configuration designed to perform a variety of different tests is proposed. This includes realistic locomotion tests, active impedance tests, collision tests, elevation tests and impact force tests—e.g., to simulate an impact between a legged robot and the ground when dropped from a specific distance or a collision between an industrial or collaborative robot and an external element.

2. Proposed Active Impedance Controller System

The motor controller system covered in this article is based on the Field Oriented Control (FOC) [17] commutation strategy further described in Appendix I. FOC enables high-efficiency, high-bandwidth control using Proportional–Integral–Derivative (PID) controllers. The system includes a plain cascaded control system architecture and includes PD and PI controllers to accomplish high-bandwidth and robust impedance, torque and field control. A complete system diagram is shown in Figure 2.

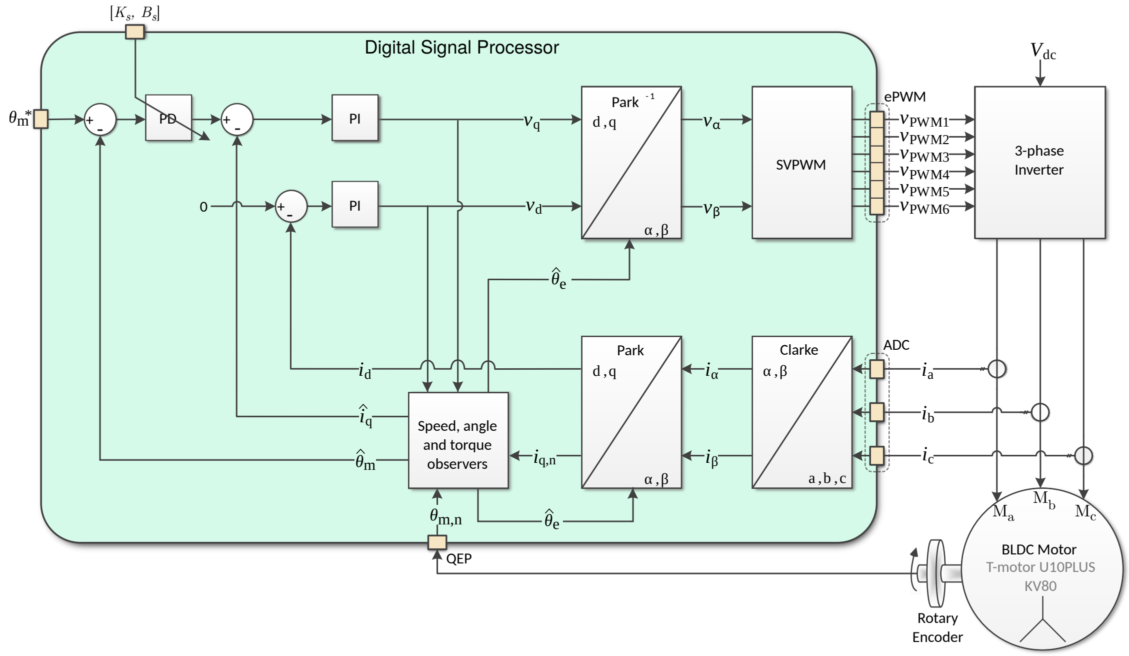

Figure 2. Simplified block diagram of the entire closed loop motor controller system, including Field Oriented Control, angle and current observers, virtual compliance and torque and field controller loops.

The outer mechanical angle (θ_m) controller loop consists of a gain scheduled PD controller which enables active impedance control (virtual compliance) further described in Section 3.2. Within that loop, there is a torque loop that uses a PI controller and the quadrature current (i_q) as feedback to ensure a certain torque response. This is further described in Section 3.1. A field loop that uses a PI controller and the direct current (i_d) as feedback ensures that no field is generated in the stator windings which ensures maximum torque/current is delivered [26]. A novel and a Luenberger/Kalman observer filter the quadrature i_q and direct currents i_d as well as the rotor angle θ_m to enable low-noise while ensuring that minimal phase delay and high-bandwidth are obtainable.

3. Motor Controller Designs

A cascaded controller architecture is used to enable active impedance control. All three loops (field, torque and impedance) are presented in the block diagram (Figure 3).

A model-based design method is proposed to design the proportional and integrator gains in the PI controllers within the field and torque loops (see Figure 3). It is based on the Nyquist frequency method and the focus is to enable high-bandwidth robust torque and field control. Another model-based method is presented to design the proportional and derivative gains in the PD controller within the impedance loop. This method is based on the pole-placement method and the parameters are designed to accomplish a dynamic response which reflects the response of a desired second order spring-damper system.

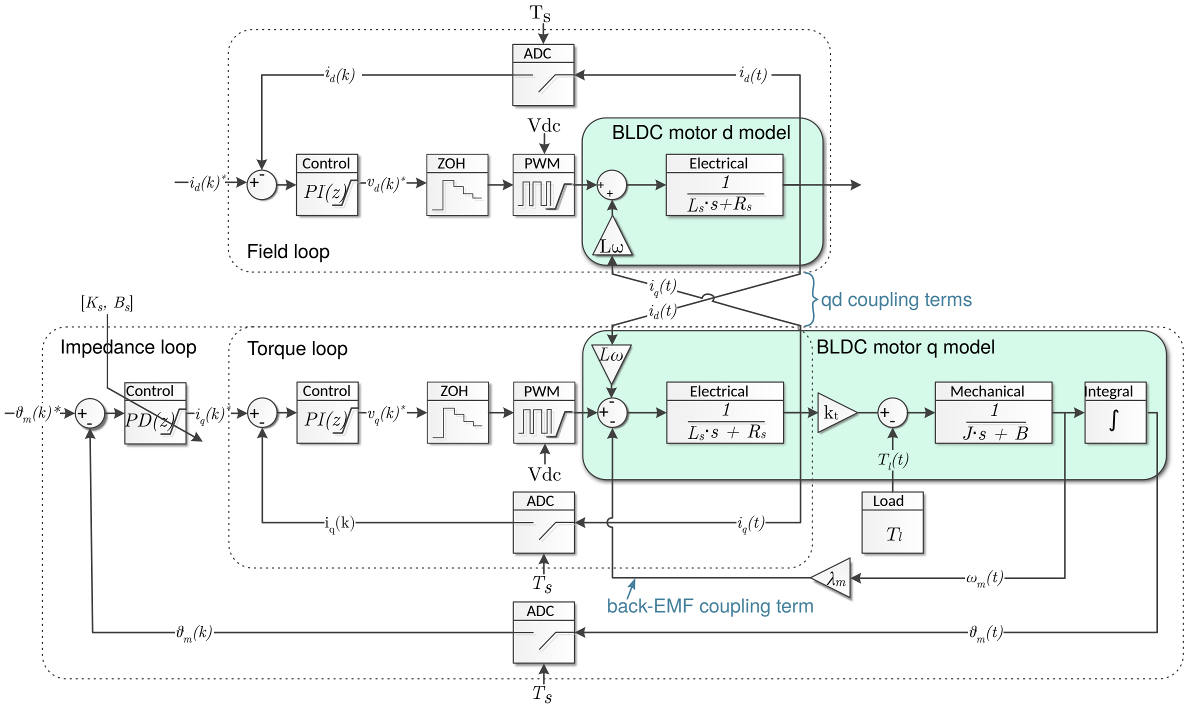

Figure 3. Simplified block diagram illustrating the rotating reference frame equivalents of the Field, Torque and Impedance loop.

3.1. Torque and Field Controller Design

The torque and field controllers are used to control the torque demanded from the higher level controller and the electromagnetic field generated across the stator windings. In this section, a controller design is proposed that is based on the standard and well-known Nyquist method and bilinear transformation as well as best practice design choices. The main purpose of this design approach is to enable high-bandwidth, low-noise, robust control. As depicted in Figure 3, the torque loop is coupled to the motor's back-Electromotive-Force (back-EMF) (back-EMF coupling term depicted in Figure 3) which creates a low frequency zero in the torque controller loop. This means that even though an integrator is applied in the controller, zero steady state cannot be obtained (assuming $\omega_m \neq 0\,\mathrm{rad/s}$). However, as the proprioceptive actuator design in compliant robotics typically involves low Revolutions Per Minute (RPM) and high torque motor drive, the back-EMF will most often be fairly small, generating a small error. In addition, the high torque controller bandwidth as well as the outer compliance loop will reject this error even further. Thus, a feedforward decoupling compensation (as described in [27]) will generate more issues, especially in terms of noise, than it will benefit for this specific application. The same logic applies to not using a feedforward decoupling compensation to decouple the field and torque loops (qd coupling terms, depicted in Figure 3).

The controller pseudo algorithms used for controlling motor torque and field are shown in (Appendix C). The decoupling terms should be left out of (A15) and (A16) if high-bandwidth (BW > 1 kHz) is required. The design method proposed in this paper is based on the Nyquist frequency method in which the trade-off between bandwidth and robustness can be selected by a desired amount of phase margin from which the parameters are designed. Designing for 60° of phase margin is proposed as it creates an unconditionally stable system while achieving high-bandwidth. Equations (A24) and (A25) are derived from the bilinear transformed motor model including sampling and delays. The derivation is shown in Appendix G. Note that the design procedure assumes that sensor delays, propagation delays, etc. are negligible. First, the zero of the integrator is designed such that it cancels out the pole of the electrical motor model $-\tau_I = -\frac{R}{L}$ which leads to approximately $-90°$ phase shift in the entire frequency spectrum (when leaving phase shift based on the low frequency zero and sampling out of the model). This way, the bandwidth is entirely restricted by the sampling and PWM delay and high-bandwidth can be achieved. The desired crossover frequency is determined by solving for ω_c^* in Equation (A24) and then solving Equation (A25).

3.2. Active Impedance Controller Design

The active impedance controller is used to compliantly control the angle of the rotor or the trajectory of the end-effector of a robot. As no specific application is focused on in this paper, a simple design methodology is proposed (based on the standard and well-known pole-placement method) that only involves controlling the compliance at the rotor shaft. For example, in a legged robot this could correspond with the hip compliance shown in Figure 4a.

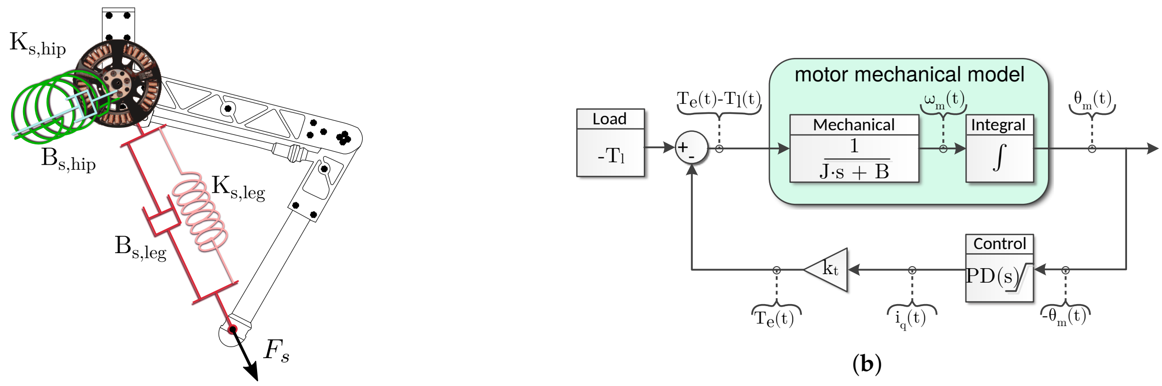

(**a**) (**b**)

Figure 4. Illustration of the hip compliance ($K_{s,hip}$, $B_{s,hip}$) and foot compliance ($K_{s,leg}$, $B_{s,leg}$) in a robot leg (**a**) and of the simplified impedance loop in relation to external force $\frac{\theta_m}{-T_l}$ (**b**). (**a**) is adopted from [10] and (**b**) is derived and simplified from Figure 3

For applications such as legged robots and collaborative robots, it is desired to control the compliance between the end-effector and the actuator (leg compliance in Figure 4a). For these applications, the forward kinematics and polar coordinate transformation described in [28] should be included in the model. The impedance obtained by the controller should be programmable in a way that enables the robot or the user to change the impedance according to a desired model which can be expressed by one of the following equations:

$$\frac{X_s(s)}{F_s(s)} = \frac{1}{M_s s^2 + B_s s + K_s} \qquad \frac{Y_s(s)}{U_s(s)} = \frac{1}{\frac{1}{\omega_n^2} s^2 + 2\zeta \frac{1}{\omega_n} + 1} \tag{1}$$

M_s, B_s and K_s represent the mass, desired damping constant and desired spring constant, respectively. ω_n and ζ are the desired natural frequency and damping factor, respectively. Either of the equations in (1) can be chosen as the reference dynamic model depending on the specific application. To be able to simplify the active impedance controller design, the impedance loop in Figure 3 is simplified to the static external load closed-loop system shown in Figure 4b. The external load torque T_l is treated as the input to this closed-loop system while the mechanical motor model is the forward path. The feedback is the product of the PD controller and the torque constant. The inner torque loop is assumed to have a much higher bandwidth than the active impedance controller meaning that it can be removed from the model. In addition, the sampling frequency is assumed to be much higher than the active impedance controller bandwidth thus the active impedance controller is designed as an analogue controller. A static situation is assumed where the desired angle is constantly zero. It is acknowledged that this is not a realistic case. However, the essence of compliance is that it should be able to absorb any external force acting on the system—for instance, a person pulling on a spring acts as an external force and the spring generates force to oppose that. Using Mason's rule, the closed-loop active impedance controller transfer function is derived:

$$\frac{\theta_{\mathrm{m}}(s)}{-T_{\mathrm{l}}(s)} = \frac{\frac{1}{Js+B}\frac{1}{s}}{1+\frac{1}{Js+B}\frac{1}{s}(\tau_{\mathrm{d}}s+1)K_{\mathrm{p}}K_{\mathrm{t}}} = \frac{1}{Js^2+(B+K_{\mathrm{p}}K_{\mathrm{t}}\tau_{\mathrm{d}})s+K_{\mathrm{p}}K_{\mathrm{t}}} \tag{2}$$

θ_{m}, T_{l}, B, J, K_{p}, τ_{d} and K_{t} are the mechanical angle, load torque, motor damping constant, moment of inertia of the rotor, active impedance controller integrator time constant and motor torque constant, respectively. Comparing the coefficients between Equations (1) and (2) reveals the analogies depicted in Table 1.

Table 1. Coefficients of the impedance loop, Mass-Spring-Damper and standard 2nd order transfer functions (Equation (1) and (2)).

Impedance Loop	Mass-Spring-Damper	Standard Form
J	M_{s}	ω_{n}^{-2}
$B+K_{\mathrm{p}}K_{\mathrm{t}}\tau_{\mathrm{d}}$	B_{s}	$2\zeta\omega^{-1}$
$K_{\mathrm{p}}K_{\mathrm{t}}$	K_{s}	1

This makes sense intuitively since moment of inertia J is essentially angular mass and the total system damping must be determined by the damping applied by the active impedance controller $K_{\mathrm{p}}K_{\mathrm{t}}\tau_{\mathrm{d}}$ and the damping constant of the motor (assuming an isolated system with no load). However, the transfer function of the PD controller which is included in Equation (2) is depicted in Equation (3).

$$G_{\mathrm{PD}} = K_{\mathrm{p}}(\tau_{\mathrm{d}}s+1) \qquad G_{\mathrm{lead}} = \frac{K_{\mathrm{p}}(\tau_{\mathrm{d}}s+1)}{\alpha\tau_{\mathrm{d}}s+1}, \alpha < 1 \tag{3}$$

As the complex frequency goes towards infinity ($s \to \infty$), the magnitude of the PD controller goes towards infinity. Hence, high frequency motor angle noise gets amplified and injected into the torque loop. Thus, the lead compensator depicted in (3) is proposed, by which a pole at $\frac{1}{\alpha\cdot\tau_{\mathrm{d}}}\left[\frac{\mathrm{rad}}{\mathrm{s}}\right]$ is placed to reduce the gain at high frequencies. This should be placed about four to 10 decades higher than the maximum possible zero $\frac{1}{\tau_{\mathrm{d}}}$ to ensure a precise damping constant as well as a suitable reduction of high frequency magnitudes.

4. Novel Observer: Mechanical Angle, Electrical Angle and Speed Filtering

As depicted in Appendix J, noise arising from the angle sensor (typically a 12-bit magnetic encoder) and the online computation of speed is injected nearly directly into the motor phases when high-bandwidth torque control is enabled. Thus, an approach to filter the mechanical angle, electrical angle and speed is needed. A novel closed-loop observer, including sensor feedback, is proposed to ensure precise estimation with minimum delay, see Figure 5. Similar to a Luenberger observer, it consists of two steps—the estimate-ahead step and the correct step.

4.1. Estimation Step

As shown in the model, Equation (A8) (in Appendix B), the quadrature voltage v_{q} includes a term that includes the magnitude of the back-EMF ($\omega_{\mathrm{m}}\lambda_{\mathrm{m}}i_{\mathrm{q}}$) which is proportional to the speed ω_{m}. Therefore, the observer estimates the speed ahead $\hat{\omega}_{\mathrm{m}}^{-}$, by using the quadrature voltage reference v_{q}^{*}, computed by the PI controller. Doing so requires the observer to subtract the voltage generated based on the internal line resistance and inductance v_{RL} from the quadrature voltage reference v_{q}^{*}. The direct way to do this is to propagate the quadrature current i_{q} through the inverse of the electrical model ($L_{\mathrm{s}}s+R_{\mathrm{s}}$). However, as the inverse electrical model includes a zero it will amplify the noise coming from the quadrature current i_{q}. Hence, a noise-reduced quadrature current estimation is computed instead by filtering the quadrature current reference i_{q}^{*} using a filter with the same bandwidth as the closed-loop torque controller. After subtracting the estimated RL voltage $\hat{v}_{\mathrm{RL}}$ from the quadrature current reference, the inverse of the peak magnetic flux $\lambda_{\mathrm{m}}^{-1}$ is multiplied with the estimated back-EMF $\hat{e}$, thereby predicting the mechanical speed.

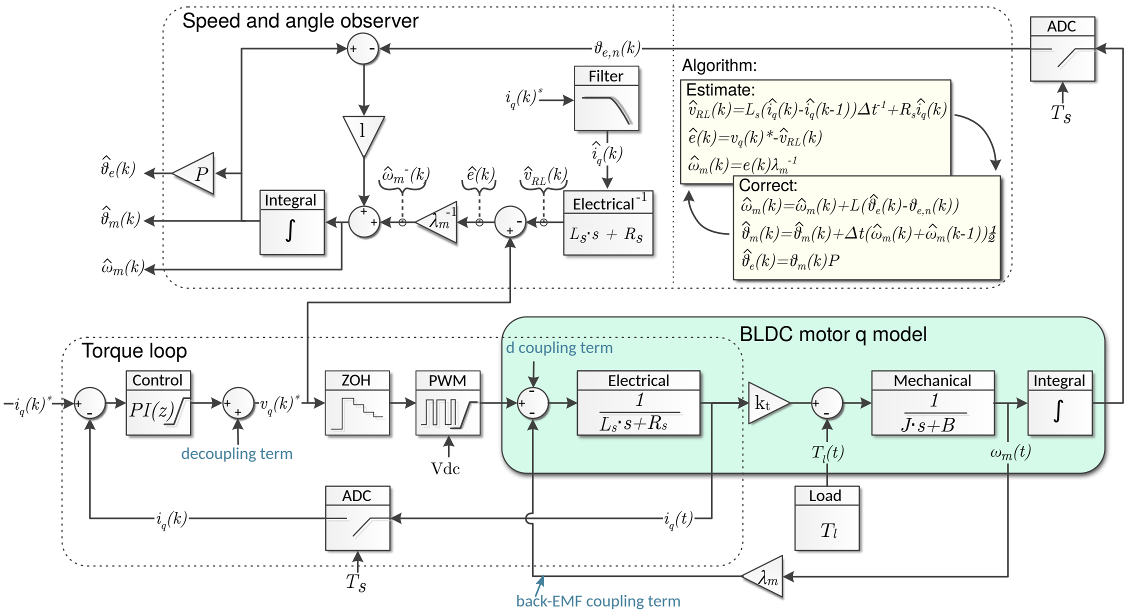

Figure 5. Illustration of the torque loop and speed and angle observer proposed in this section. The light-yellow boxes outline the algorithms used for the observer. The decoupling term is proposed to be 0 V but can be included if needed.

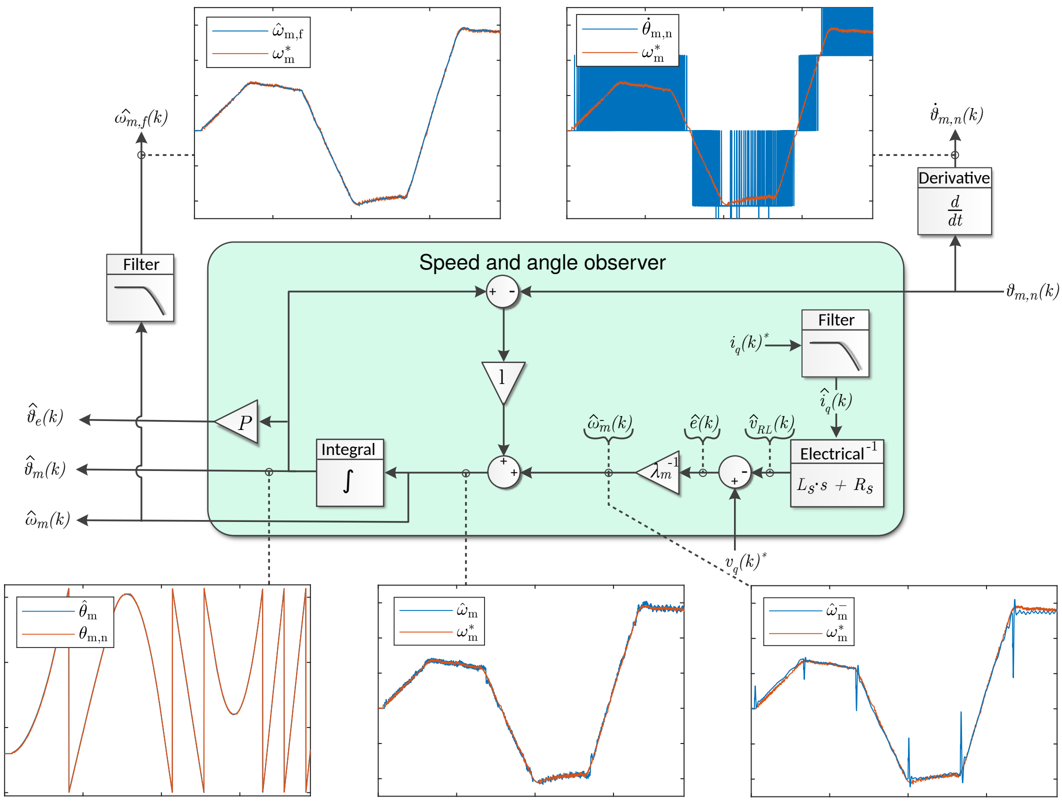

Figure 6. Illustration of the speed and angle observer including test results of the internal parameters. The first axis of all plots relates to time. The reference speed ω_{m}^{*} is an estimate of the true speed, which is calculated by applying a 200 Hz low-pass filter to the derivative of the raw angle $\dot{\theta}_{\mathrm{m,n}}$ and then offset in time with an amount corresponding with the time-delay introduced by the filter.

The results shown in Figure 6 suggest that the observer provides good open-loop estimation (graph in lower right corner) of speed with enhanced high-frequency noise response in relation to that obtained by taking the derivative of the angle (graph in upper right corner), directly measured by the sensor. Note that the spikes of the speed estimated ahead $\hat{\omega}_{\mathrm{m}}^{-}$ occur due to the big step in torque reference (by which the observer becomes very sensitive to model uncertainties). This will never occur in compliant robotics where the robot is operated in angle mode using the impedance loop instead of torque mode.

4.2. Correction Step

Assuming that the speed and angle obtained from the sensor provides the best low-frequency response (closest to the true angle and speed) and the worst high-frequency response (high-noise contribution), a correction step should be applied that ensures the observer tracks the low-frequency response of the sensor (the true angle) while including the low-noise (high-frequency response) of the estimation ($\hat{\omega}_{\mathrm{m}}^{-}$). This should be enabled by the correction loop in the observer. Applying the superposition principle to the correction loop in Figure 5 and including the a priori estimate of the angle θ_{m}^{-} into the output with respect to estimation loop, the two loops can be derived (Figure 7).

(**a**) (**b**)

Figure 7. Simplified block diagram of the output vs. measurement loop $\frac{\hat{\theta}_{\mathrm{m}}(k)}{\theta_{\mathrm{m,n}}(k)}$ (**a**) and the output vs. estimation loop $\frac{\hat{\theta}_{\mathrm{m}}(k)}{\hat{\theta}_{\mathrm{m,n}}^{-}(k)}$ (**b**).

Applying Mason's formula to both loops, the closed-loop response in the laplace-domain of each loop is approximated:

$$\frac{\hat{\theta}_{\mathrm{m}}(s)}{\hat{\theta}_{\mathrm{m}}^{-}(s)} = \frac{s}{s-l} \qquad \frac{\hat{\theta}_{\mathrm{m}}(s)}{\theta_{\mathrm{m,n}}(s)} = \frac{l}{s-l}$$

It is evident that the correction step outputs a combination of the high-frequency response of the estimation and the low-frequency response of the sensor which is required in order to achieve noise-reduced estimation with low time delay (see graph in the middle lower graph in Figure 6).

This correction is essentially a first order Finite Impulse Response (FIR)-filter which determines the corrected estimated speed $\hat{\omega}_{\mathrm{m}}$ by weighing the initial guess (the estimated angle $\hat{\omega}_{\mathrm{m}}^{-}$) against the measured angle $\hat{\theta}_{\mathrm{m,n}}$. The estimated mechanical angle $\hat{\theta}_{\mathrm{m}}$ is calculated by taking the integral to the corrected speed $\hat{\omega}_{\mathrm{m}}$ and the electrical angle $\hat{\omega}_{\mathrm{e}}$ is estimated by multiplying the estimated mechanical $\hat{\theta}_{\mathrm{m}}$ angle with the motor pole pairs P (graph in the left lower graph in Figure 6).

The observer gain l may be designed by placing the pole using the observer error dynamic equation:

$$e(k+1) = -le(k)$$

Using this observer, high-accuracy, low-noise is obtained when low-speed is required. However, high-speed may lead to a non-linear relationship between the quadrature voltage v_{q} and speed (especially if over-modulation occurs) which could lead to observer diversion, thus, controller instability. A solution to this could either include increasing the observer gain l when speed increases so that the observer trusts the measurements more at high-speed. Otherwise, the observer gain l may be changed into a PI controller which includes enhanced low-frequency tracking response.

5. Kalman/Luenberger Observer: Quadrature Current Filtering

As depicted in Appendix J, the noise appearing in the quadrature current is mainly determined by the current sensors. Hence, the novel observer presented earlier has only a small influence on the quadrature current noise. Therefore, another observer is proposed which aims to reduce this without considerably reducing the bandwidth of the torque and field controllers. The proposed method is based on the two standard and well-known observer methods, the Luenberger observer and the Kalman filter. The gain may either be deterministically (Luenberger [29]) or stochastically (Kalman [30]) derived. The observer is shown in Figure 8.

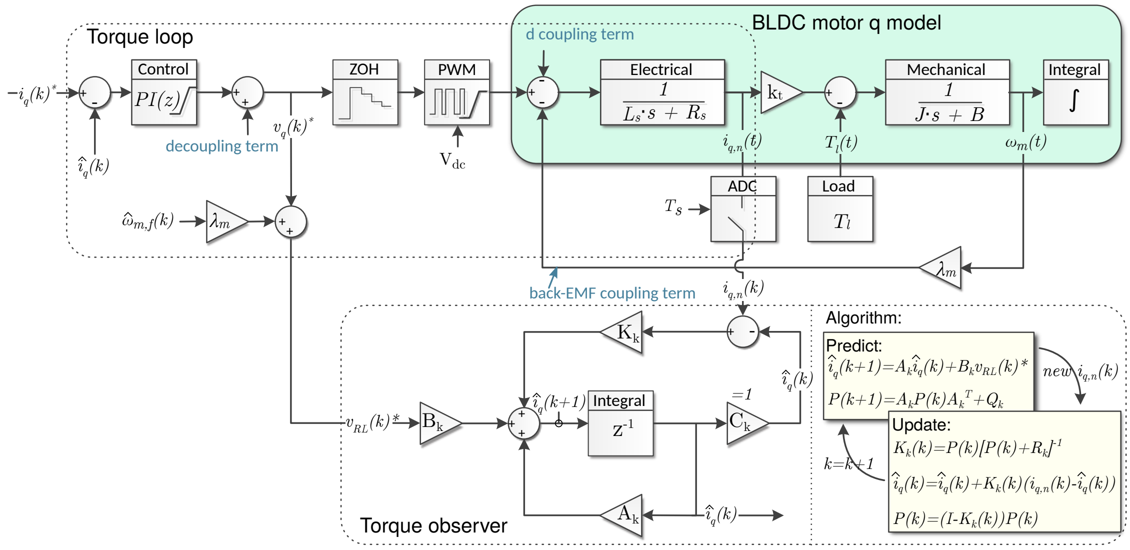

Figure 8. Illustration of the torque loop and torque observer proposed in this section. The light-yellow boxes outline the algorithms used for the observer. The decoupling term is proposed to be 0 V but can be included if needed.

The observer calculates the reference voltage that is applied across the internal line resistance and inductance v^*_{RL} by subtracting the back-EMF coupling term (shown in Figure 3) from the quadrature voltage reference v^*_{q}. This is used to estimate the quadrature current i_{q} ahead by using the first order discretized state-space model of the voltage/current relationship in the internal RL circuit of the motor:

$$\dot{i_{\mathrm{q}}}(t) = \overbrace{-\frac{R_{\mathrm{s}}}{L_{\mathrm{s}}}}^{A} i_{\mathrm{q}}(t) + \overbrace{\frac{1}{L_{\mathrm{s}}}}^{B} v_{\mathrm{RL}}(t) \tag{4}$$

R_{s}, L_{s}, A and B are the internal line-resistance, internal line-inductance, state-transition gain and input gain, respectively. When a new measurement arrives, the quadrature current estimation is corrected by weighing the predicted estimate (apriori estimate $\hat{i}_{\mathrm{q}}(k+1)$) against the measured quadrature current $i_{\mathrm{q,n}}$. A high Kalman gain K_{k} results in increased trust in the measurement with decreased trust in the estimate and vice-versa. Q_{k} and R_{k} is the variance of the noise arising in the quadrature voltage estimation and measured quadrature current, respectively. They can both be determined by measuring the noise in the system at steady-state (preferably at 0 A). The Kalman gain is determined such that the Mean Squared Error ($P(k)$) goes towards zero, hence the noise is optimally filtered. However, instead of the stochastic derivation of the Kalman gain, one may instead choose to determine a fixed Luenberger gain L_{k} which can be done in a number of ways [31,32]. One way to do this is by placing the pole of the observer, using the observer error dynamic equation:

$$e(k+1) = (A_k - L_k C_k)e(k) \quad (5)$$

e is the observation error. The output gain C_k, the discrete state transition gain A_k and the input B_k can be estimated using Equation (A9) (in Appendix B).

6. Experimental Test Setups

During all experiments, the motor module including test stand, T-motor U10PLUS KV80 and controller PCB (illustrated in Figure A5) are used and a DC voltage supply (TENMA 72-2640) is used to supply the motor controller PCB with 25 V. All static parameters used for the experiments are shown in Table A1. The real hardware as well as all experimental setups can be observed in Figure 9. Appendix L includes a description of the electronics and software developed and implemented for the motor controller.

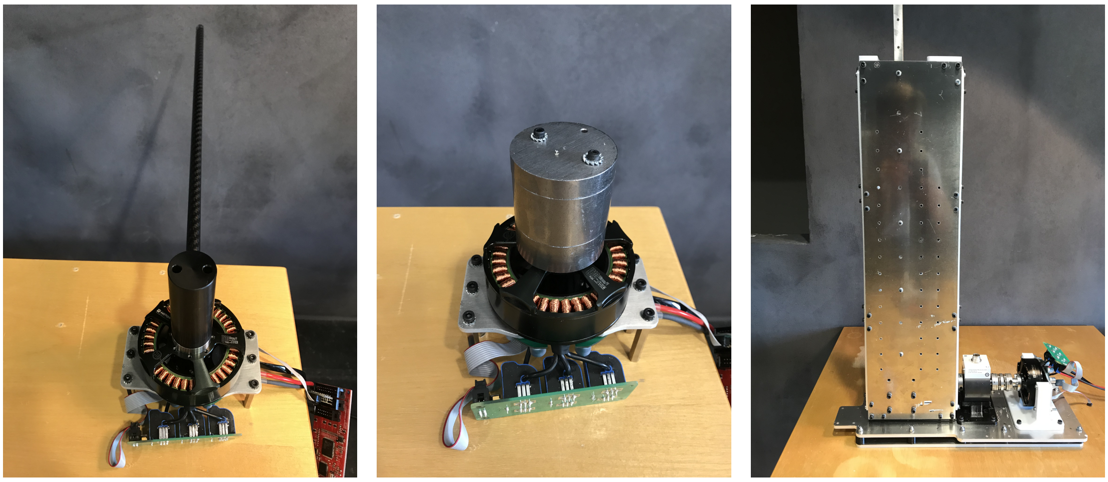

(**a**) (**b**) (**c**)

Figure 9. Photos of the hardware used for the experiments.

(a) **1-link load** includes a 30 cm carbon fiber tube (propeller) attached to the motor shaft through a hollow cylindric plastic spacer. The purpose of this configuration is to demonstrate active impedance by applying external force to the propeller

(b) **Inertia load** includes a 900 g cylindric iron load directly attached to the motor shaft. The purpose of this setup is to demonstrate the proposed controller including a fixed level of attached inertia.

(c) **Impact load** includes a weight which is mounted on a linear rail. The motor is connected to another rail through a torque sensor (T22/20NM), two mechanical couplings and a spur gear. The purpose of this setup is to demonstrate how the motor controller complies during impact force.

7. Experimental Results and Discussion

7.1. Experimental Results: Active Impedance Controller Compared with Dynamic Impedance Model

For these tests, the 1-link loadexperimental setup shown in Figure 9a, is used. The motor is driven in active impedance control mode with a fixed angle reference. Then, the shaft is forced out of the desired angle by rotating the propeller πrad(using an external force). The propeller is then released, allowing the controller to rotate the propeller back to the desired angle. This experiment is performed eight times using the eight different impedance characteristics listed in Table A2. The results from the experiments are shown in Figure 10a,b.

As can be seen, the experimental results roughly match the mathematical models. Small deviations occur, both regarding the natural frequency and damping factor. As the natural frequency in a standard 2nd order under-damped rotational system mostly depends on the moment of inertia and the spring constant, the estimated inertia may be a bit off. The assumption of an infinite torque bandwidth may have an impact on the spring constant as well. The discrepancy of the damping may be caused by an inaccurate inertia estimation or by un-modeled damping in the system. These results highlight the importance of accurate estimation of the physical parameters (inertia, damping factor, etc.) and that the accuracy of the active impedance controller design depends on how close the impedance bandwidth is to the lead compensator and closed-loop torque controller poles.

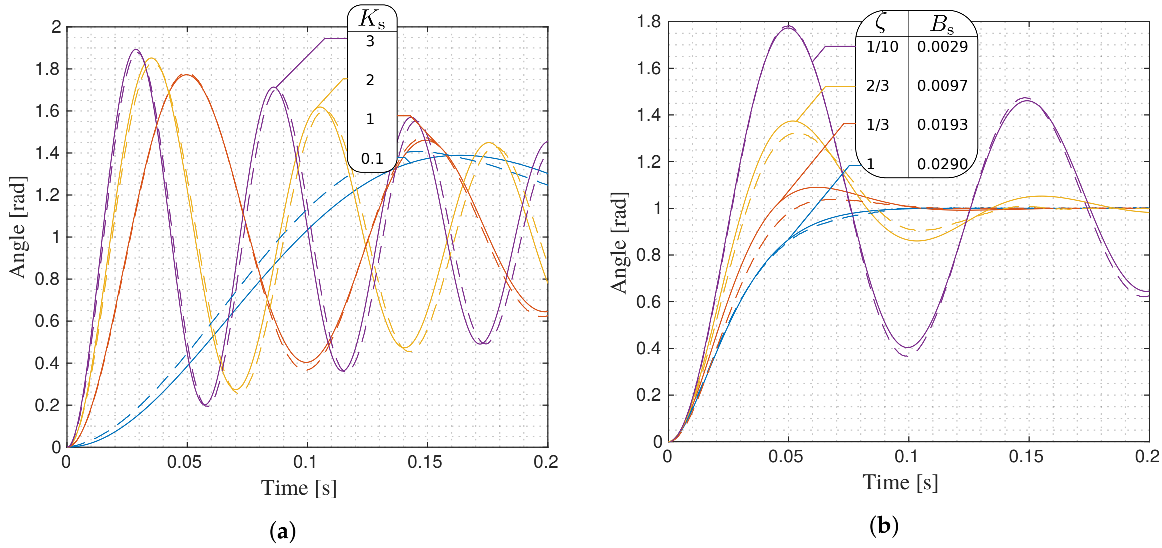

Figure 10. Measured (dashed lines) and simulated (solid lines) results from eight experiments (listed in Table A2) conducted on the active impedance controller. The spring constant is varied in (**a**) and the damping constant is varied in (**b**). The measured results are offset and scaled to match the amplitude and start angle of the simulated.

Note, two videos showing the conducted experiments and their results are available as supplementary materials—with (Video S10) and without observers (Video S9).

7.2. Experimental Results: Torque Control—Angle and Speed Observer vs. no Observer

This experiment is conducted to show the results from deploying the novel angle and speed observer described in Section 4. The experiment is conducted under zero load as this results in high torque specific acceleration. This demands a lot from the observer, especially in terms of stability and accuracy. The motor controller is configured to run with torque control and a multiple torque reference step profile is applied. The results are shown in Figure 11. The torque rise time of about 133 µs, depicted in Figure 11a,b shows that high-bandwidth (approximately 2.6 kHz) is accomplished while relatively low overshoot occurs, verifying high robustness. This bandwidth is not as high as the torque controller bandwidth in the MIT Cheetah Mini (4.5 kHz) [12]. The main reason for this is that the MIT Cheetah Mini is using the STM32F446 microcontroller, which enables twice the clock frequency than the TMS320F28069 (used in this project). Therefore, MIT are capable of running the controller loop at a sample rate of 40 kHz whereas 25 kHz is used in this work. However, the controller design proposed in this paper can deliver approximately the same bandwidth in relation to sample rate as enabled in the MIT Cheetah Mini. It must be emphasized that this bandwidth can be adjusted by adjusting the phase margin, where 60° is used in this case to enable highly robust control. A large noise reduction can be observed in the speed ω_m, direct current i_d and phase voltages. As quantified by the noise analysis (Appendix J), using the noise-reduced estimated electrical angle greatly reduces the noise appearing in the direct-current which then reduces the noise on the phase voltages. It should be emphasized that the effect of the noise reduction is even more noticeable when using active impedance control and/or back-EMF feedforward. The reason for this is that the noise is then amplified (based on the speed calculation) and afterwards injected into the system (based on the high-bandwidth torque control).

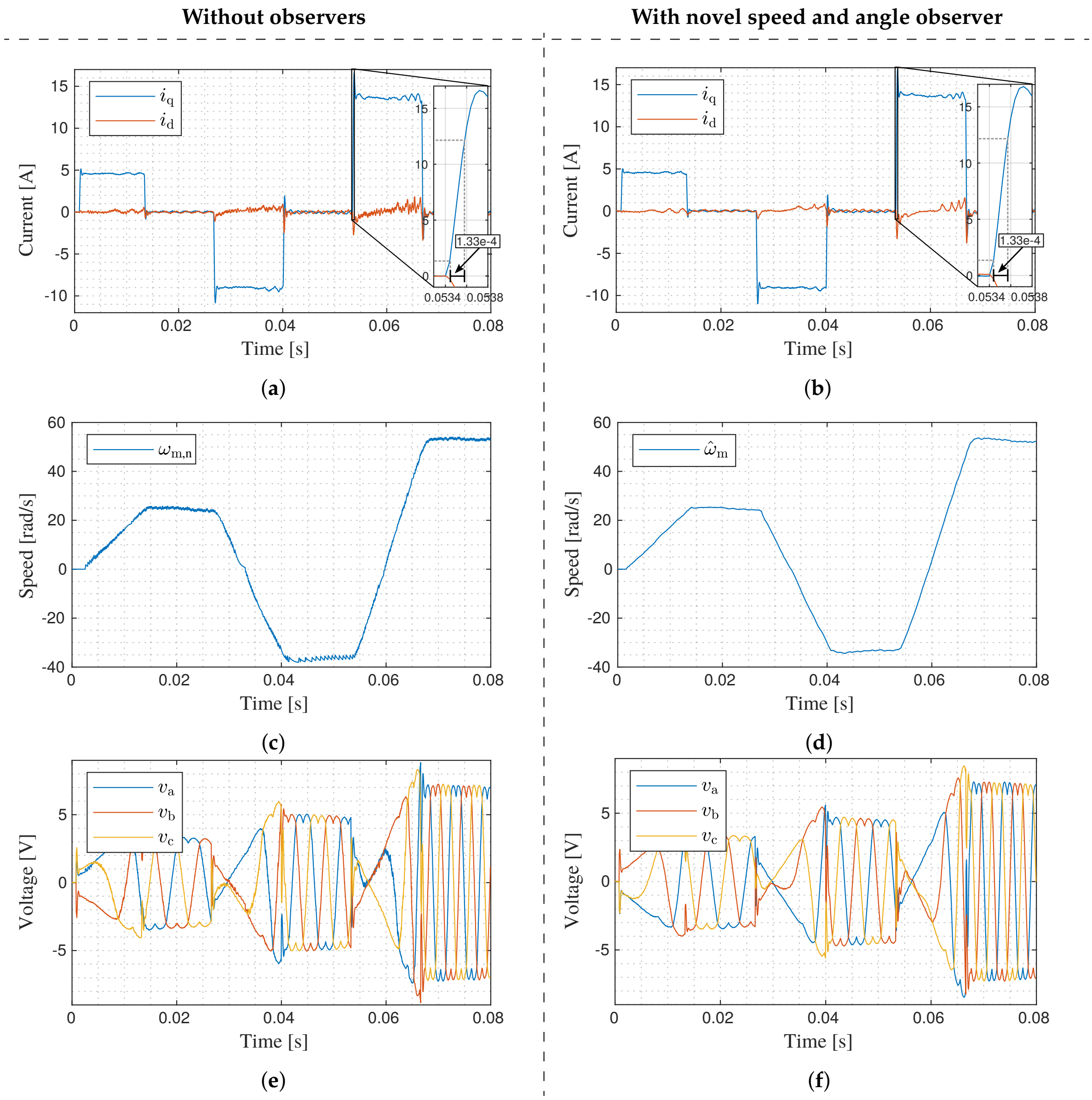

Figure 11. Measured and estimated results from two conducted experiments using torque mode with multiple step in torque reference with zero load—without observer (**a**,**c**,**e**) and with the novel angle and speed observer (**b**,**d**,**f**). The torque rise times are depicted on (**a**,**b**). Both speed estimations $\omega_{m,n}$ and $\hat{\omega}_m$ are filtered with the same low-pass filter including a 3 dB bandwidth of 200 Hz for better performance visualization.

Further investigation of the angle and mechanical observer performance is shown in Figure 12 both with (Inertia load) in Figure 9b) and without load.

As shown in Figure 12a,b, the main noise contribution arising in the 12-bit encoder is quantization noise. Therefore, the observer includes the effect of providing a higher resolution angle (both with and without load) than is provided by the sensor alone. One may argue that similar results may be obtained by picking a higher resolution magnetic encoder. However, today's off-the-shelf high-end magnetic encoders are typically 12–14 bit, where the 14-bits encoders include noise on the two least significant bits meaning that the effective resolution is reduced to about 12 bits. The high frequency noise gets amplified when speed is calculated which is clearly depicted in Figure 12c. The observer is again capable of delivering a highly reduced noise response (both with and without load). A standard low-pass filter with the same amount of filtering would cause a huge phase-delay which the observer clearly does not. Therefore, it can be concluded that the proposed novel observer is capable of greatly reducing noise in the system while maintaining a high-bandwidth and highly robust closed-loop torque control.

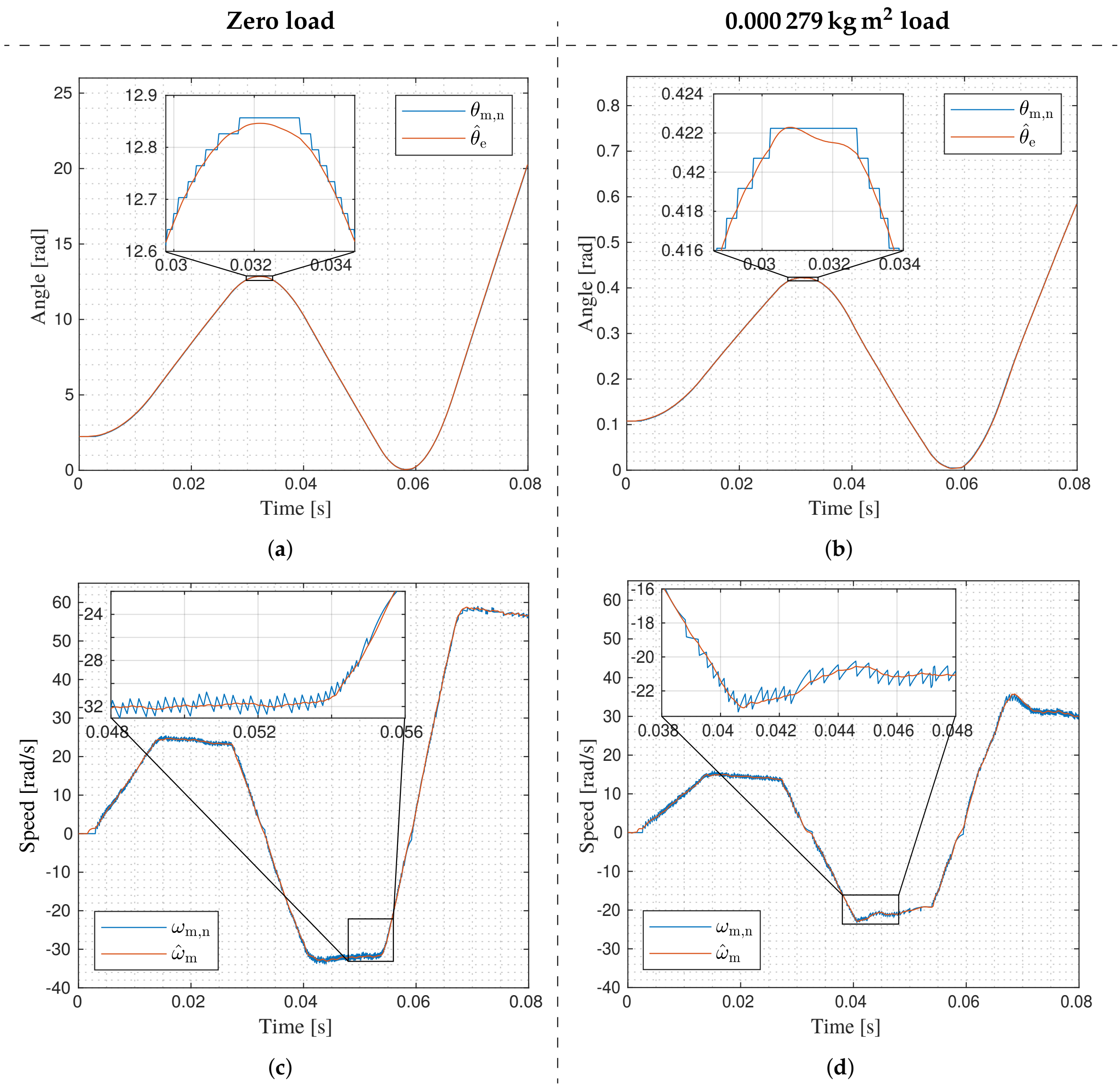

Figure 12. Measured and estimated results from the conducted experiment using torque mode with multiple step in torque reference with zero load (**a**,**c**) and with 0.000 279 kg m^2 (**b**,**c**)—including the novel angle and speed observer. The zoomed areas depict the noise reduction and dynamic capabilities of the observer. Both speed estimations $\omega_{m,n}$ and $\hat{\omega}_m$ are filtered with the same low-pass filter including a 3 dB bandwidth of 200 Hz for better performance visualization.

To illustrate the behavior of the novel speed and angle observer, the intermediate results as well as the final output of the observer are shown in the observer diagram, see Figure 6. This behavior is further described in Section 4.

7.3. Experimental Results: Torque Control—Torque Observer vs. no Observers.

This experiment is conducted to investigate the performance of the torque observer proposed in Section 5. The motor controller is configured for torque control and multiple torque reference steps are performed. The results are shown in Figure 13.

As shown, high-frequency noise appearing on the quadrature current $i_{q,n}$ (directly derived from noisy measurements) is significantly reduced by the observer $\hat{i}_q$. However, small discrepancies (offset errors) occur which are determined by model inaccuracies. However, the effect of this quadrature current discrepancy should not be significant when using active impedance control as the outer loop compensates for this issue.

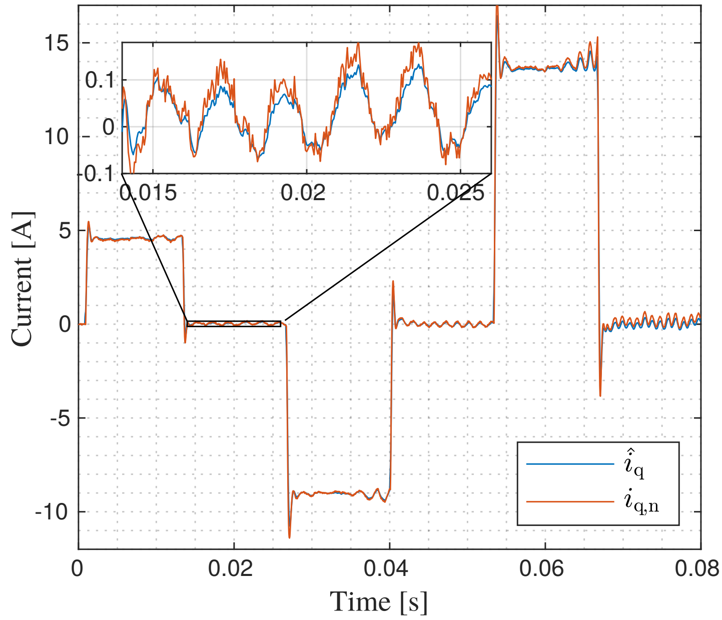

Figure 13. Measured and estimated results from the conducted experiment using torque mode with multiple step in torque reference with zero load—including the novel angle and speed and the Kalman/Luenberger observer. The zoomed areas depict the noise reduction capabilities of the Kalman/Luenberger observer.

7.4. Experimental Results: Speed Control—Angle, Speed and Torque Observer vs. no Observers

This experiment is conducted to investigate the performance of the entire proposed observer strategy including both the torque and speed/angle observers. Again, the test is conducted with zero load. The results are shown in Figure 14.

The effect of both observers on noise is consistently noticeable on all collected data. Figure 14g,h quantify a significant reduction in noise of approximately 13.5 dB which corresponds with almost five times reduction. However, a small deviation occurs in the dynamic response of speed ω_m and the quadrature current i_q which could be a result of small inaccuracies in the torque observer model.

The author of [12] noticed audible noise in the motor module at 4.5 kHz and therefore decided to perform experiments at 1 kHz instead. By using the observers, proposed in this paper, this noise will be greatly reduced and the bandwidth of 4.5 kHz can therefore be retained.

Note that two videos showing the conducted experiments and their results are available as supplementary materials (the flywheel in the videos is not connected in this experiment)—with (Video S10) and without observers (Video S9). Additionally, the tests have been conducted with variable speeds (Video S5 and S6) and with load 3 N m (Video S3 and S4).

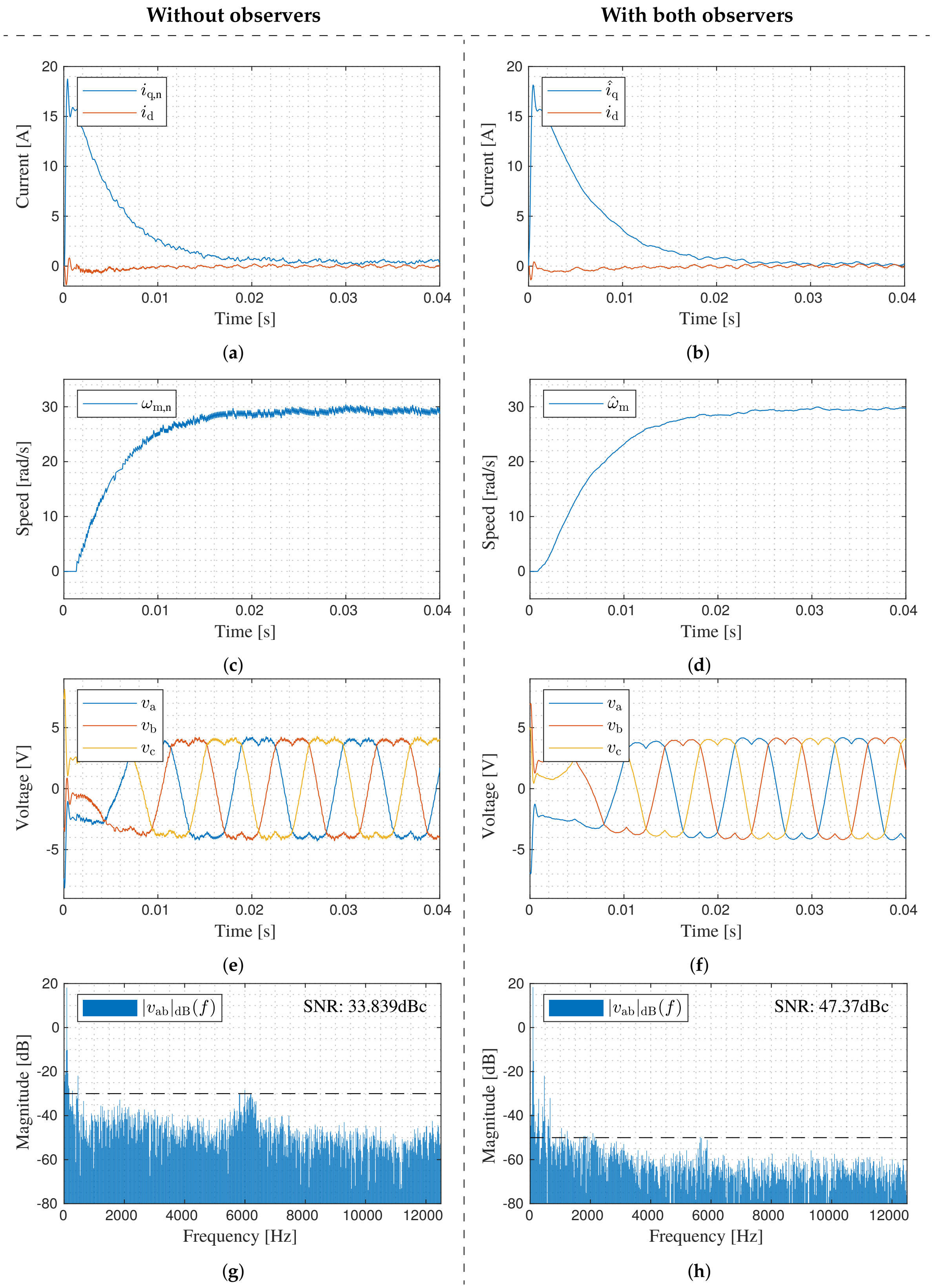

Figure 14. Measured and estimated results from two conducted experiments using speed mode with a single step in speed reference with zero load—without observer (**a**,**c**,**e**,**g**) and with both the novel angle and speed and the Kalman/Luenberger observers (**b**,**d**,**f**,**h**). Both speed estimations $\omega_{\mathrm{m,n}}$ and $\hat{\omega}_{\mathrm{m}}$ are filtered with the same low-pass filter including a 3 dB bandwidth of 200 Hz for better performance visualization.

7.5. Experimental Results: Active Impedance Control with Angle/Speed and Torque Observers—Impact Force Load

This experiment is conducted to showcase the results from using the novel impact force load as well as the performance of the motor controller during impacts. The impact force load shown in Figure 9c is used, where a 3 kg iron mass is connected to the linear rail and released at a distance from the impact block of 30 cm. The impedance model and controller parameters are listed in Table A3. The resulting torque, speed and angle are depicted in Figure 15.

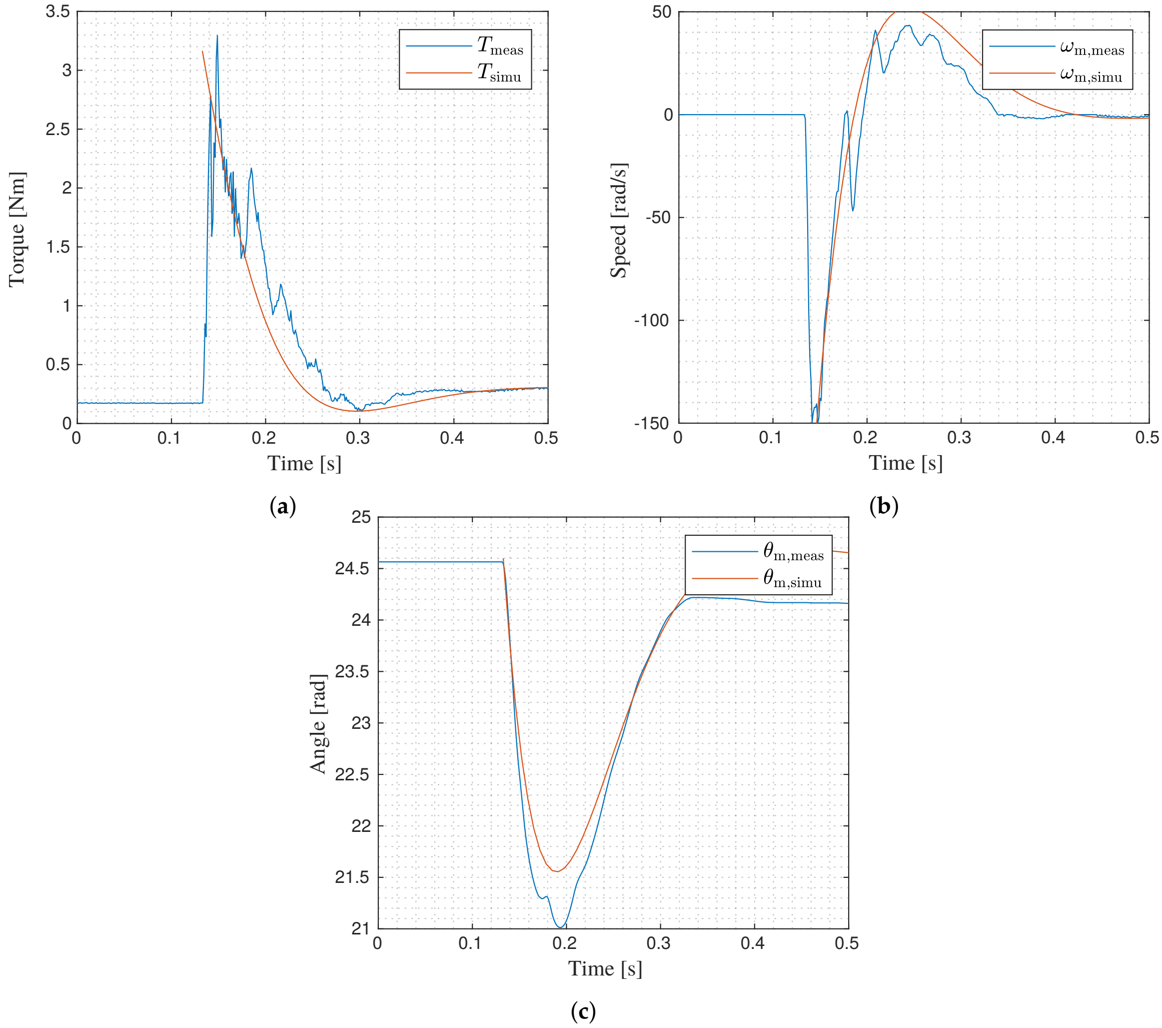

Figure 15. Measured (T_{meas}, $\omega_{\mathrm{m,meas}}$ and $\theta_{\mathrm{m,meas}}$) and simulated (T_{simu}, $\omega_{\mathrm{m,simu}}$ and $\theta_{\mathrm{m,simu}}$) results from the experiment (listed in Table A3) conducted on the active impedance controller (**a**) T_{meas}, (**b**) $\omega_{\mathrm{m,meas}}$, (**c**) $\theta_{\mathrm{m,meas}}$. The load configuration, proposed in Appendix K, is used with 3 kg mass released from a distance of 10 cm. The simulated results are offset and scaled to match the amplitude and start angle of the measurements. The torque T_{meas} is estimated from the quadrature current by $T_{\mathrm{meas}} = K_{\mathrm{t}} i_{\mathrm{q}}$.

Again, relatively high correlation between the mathematical model and the experimental results can be observed. The controller is capable of achieving impact force mitigation similar to that provided by the model. In addition, the controller runs stable and smoothly throughout the impact which sums up the controller and observer designs as high-performance. However, oscillations occur—this is one of the by-products of structural compliance resulting from the mechanical couplings depicted in Figure A3. Aside from the oscillations, structural compliance reduces torque transparency which results in lowering the force bandwidth at the end-effector. This is an issue in high-bandwidth requiring robotics. Hence, it must be emphasized that the structural compliance should be kept as low as possible for such applications. One way to reduce this issue is to include the robot kinematics and dynamics in the active impedance controller loop and employing an adaptable Kalman filter to estimate the Jacobian matrix online, as proposed and verified in [33]. Otherwise, the structural compliance can be reduced by using mechanical reinforcements or by choosing stiff materials.

Note that the two videos showing the conducted experiments and their results are available as supplementary materials—with stiff (Video S7) and soft active impedance control (Video S8).

7.6. Experimental Results: Active Impedance Control with Angle/Speed and Torque Observers—Compliance Test

Two experiments are conducted to show how the active impedance controller, including both observers, performs during a human-robot collision. For these tests, the 1-link load shown in Figure 9a is used. A sinusoidal angle reference is applied to the active impedance controller. Then, after a few cycles, a human hand is positioned between the start and end angle in the trajectory path for about three cycles, which ensures three collisions. This test was conducted two times—once with reduced torque controller bandwidth (50 Hz) and once with the originally designed torque controller (2.6 kHz). The reduced bandwidth of 50 Hz is arbitrarily chosen to show the importance of high torque bandwidth control when deployed as inner loop in an active impedance controller. [10] describes in detail the relationship between the torque controller bandwidth and the performance of active impedance control. The results are shown in Figure 16. It can be observed that when using the reduced torque bandwidth, active the impedance controller is unable to perform a precise reference tracking. Additionally, during impacts (gray areas), the active impedance controller is unable to mitigate the impact force, as high quadrature current spikes occur. Using the high-bandwidth torque controller designs, proposed in this article, the active impedance controller is capable of performing a precise reference tracking as well as absorbing the impact force. It must be emphasized, that in many cases, such as slow robot motion or low active impedance control bandwidth, 50 Hz may be adequate. However, in the case of high bandwidth interaction (e.g., cobot-human collision at fast motion or fast locomotion of legged robots), the high bandwidth is critical in order to ensure no damage occurs to the robot or the environment.

Note that two videos showing the conducted experiments and their results are available as supplementary materials—with low torque bandwidth (Video S11) and high torque bandwidth (Video S12).

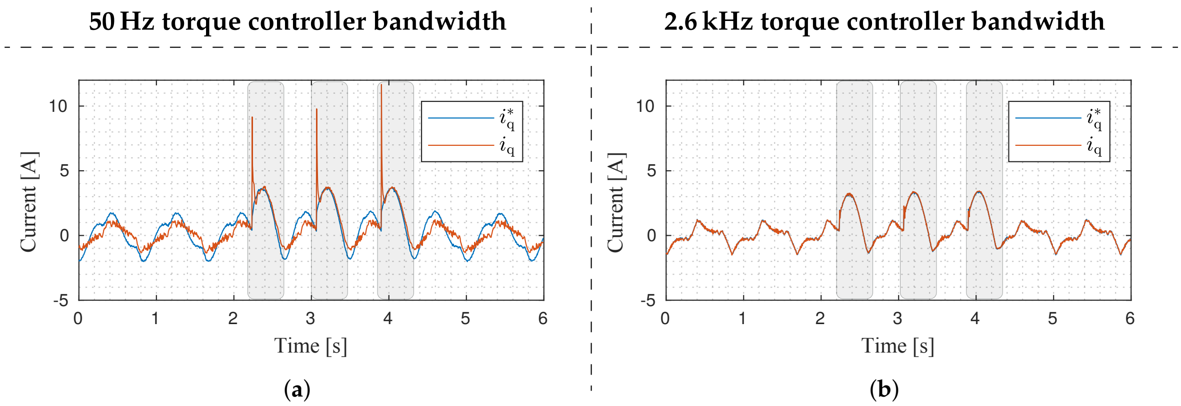

Figure 16. *Cont.*

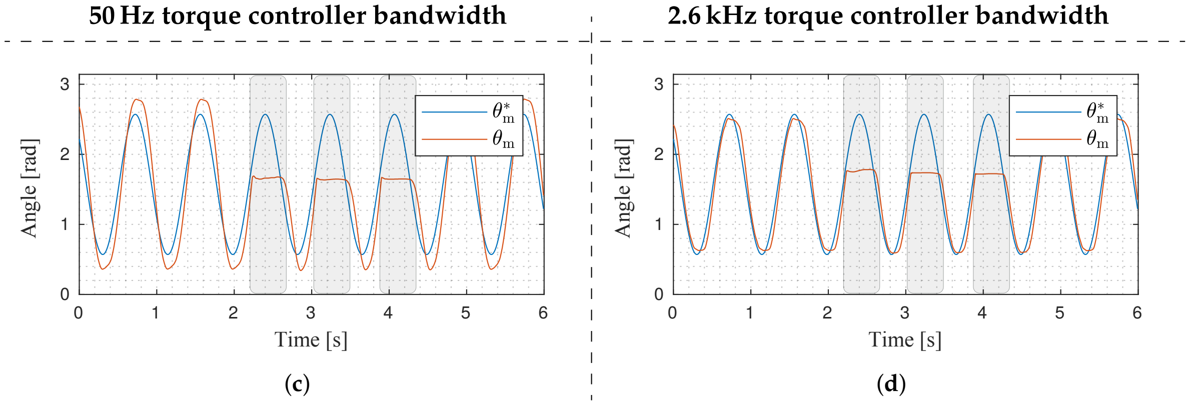

Figure 16. Measured and estimated results from two conducted experiments using active impedance mode with a sinusoidal angle reference and with a 30 cm propeller. (**a**,**c**) is at reduced torque controller bandwidth (50 Hz) and (**b**,**c**) is at the originally designed torque controller (50 Hz). Both tests are performed including both the novel angle and speed observer and the torque observer. The three gray areas on each plot depict three human-robot collisions. These are performed by putting a human hand in the middle of the trajectory path for about three trajectory cycles.

8. Conclusions

In this work, a complete controller design scheme for high-bandwidth active impedance control of compliant robotics have been presented.

Design equations, which enables calculation of the parameters in the outer active impedance control loop (PD controller), is derived in Section 3.2. In Section 7.1, the design equations was shown to be precise for a variety of different spring constants and damping factors. However, the precision of the method is highly dependent on the precision of the used passive parameters (inertia, damping factor, etc.) and how close the impedance bandwidth is to the lead compensator and closed-loop torque controller poles.

In Section 3.1, design equations as well as best practice design of the field and torque loops are proposed. As verified in Section 7.2, the torque loop was capable of fast reference tracking (about 2.6 kHz closed-loop bandwidth) while the field loop was capable of keeping the field at zero. This bandwidth is not as high as the torque controller bandwidth in the MIT Cheetah Mini (4.5 kHz) [12]. The main reason for this is that the MIT Cheetah Mini is using the STM32F446 microcontroller which enables twice the clock frequency than the TMS320F28069 (used in this project). Therefore, it is capable of running the controller loop at a sample rate of 40 kHz whereas 25 kHz is used in this work. However, the controller design proposed in this paper enables approximately the same bandwidth in relation to sample rate as enabled in the MIT Cheetah Mini. It must be emphasized that this bandwidth can be adjusted by adjusting the phase margin, where 60° is used in this case to enable highly robust control.

In Appendix J, the noise in a Field-Oriented Controlled BLDC motor was analyzed. This showed that the noise appearing on the quadrature current (in the torque loop) can be significantly reduced by reducing the noise on measured phase currents. In addition, the noise appearing in the field and impedance loop can be reduced by reducing noise on the measured rotor angle.

To address this, a Kalman/Luenberger observer was proposed to reduce noise in the torque loop and a novel speed and angle observer was proposed to reduce noise in the impedance and field loops. Section 7.2 showed that the novel angle and speed observer was capable of greatly reducing noise arising in the angle sensor (or increasing the resolution) at rotor speed at least up to 60 rad/s while no noticeable delay occurred (as it would with a low-pass filter). This was shown to be the case both at zero load and at 0.000 279 kgm^2. Section 7.3 showed a great noise reduction on the quadrature current is achieved when deploying the torque observer. Section 7.4 showed that by using both observers 13.5 dB (about five times reduction) noise reduction is facilitated, which concludes that the combination of high-bandwidth low-noise torque control of a BLDC motor has been achieved. The author of [12] noticed audible noise in the motor module at 4.5 kHz and therefore decided to perform experiments at 1 kHz instead. Using the observers, proposed in this paper, this noise will be greatly reduced and the bandwidth of 4.5 kHz can therefore be retained.

Sections 7.5 and 7.6 showed that the entire controller scheme, including all three loop designs and both observers, was capable of performing well during demanding impact force tests. Additionally, Section 7.6 includes both a test using a reduced torque controller bandwidth (50 Hz) and the original bandwidth. The results highlight the importance of high closed-loop torque bandwidth, as the reduced bandwidth was not capable of tracking the angle reference or absorbing the impact force properly.

Supplementary Materials: The following are available online at http://www.mdpi.com/2076-0825/8/4/71/s1:

- Video S1: 30 rad/s speed step test without observers (0 N m load)
- Video S2: 30 rad/s speed step test with observers (0 N m load)
- Video S3: 30 rad/s speed step test without observers (3 N m load)
- Video S4: 30 rad/s speed step test with observers (3 N m load)
- Video S5: Multi speed step test without observers (0 N m load)
- Video S6: Multi speed step test with observers (0 N m load)
- Video S7: Impact force test (stiff control)
- Video S8: Impact force test (soft control)
- Video S9: Active impedance control test without observers
- Video S10: Active impedance control test with observers
- Video S11: Human-robot collision test low bandwidth
- Video S12: Human-robot collision test high bandwidth
- C code S13: Entire motor controller source code
- PCB files S14: Motor Module 10S

Supplementary videos guide: Note, that the audio should be turned on when playing the videos. In Video S1, S2, S3, S4, S5 and S6 the viewer should notice much lower noise levels in the tests including observers—on the torque and speed graphs as well as the audio—while the dynamic response is similar which verifies the noise reduction provided by the observers. In video S7 and S8, notice that the controller is capable of repeatedly "absorbing" similar impact forces (see the torque graph) using two different spring-mass-damper characteristics (stiff and soft control). In Video S9 and S10, notice that the observers are capable of reducing noise—noticeable on the speed and torque graphs as well as the audio—when actively controlling the impedance. In Video S11 and S12, notice that at low bandwidth, the actual torque is not in sync with the reference torque, which causes the actual position to become out of sync as well. In addition, torque spikes appear during impacts, which emphasizes the importance of high torque bandwidth.

Author Contributions: Conceptualization, S.H.J.L.; Formal analysis, S.H.J.L.; Investigation, S.H.J.L.; Methodology, S.H.J.L.; Project administration, L.B.L.; Software, S.H.J.L.; Supervision, L.B.L.; Validation, S.H.J.L.; Visualization, S.H.J.L.; Writing—original draft, S.H.J.L.; Writing—review & editing, P.B. and L.B.L.

Funding: This work was partially supported by the Human Frontier Science Program under Grant agreement no. RGP0002/2017.

Acknowledgments: We acknowledge Carsten Albertsen and Cao Danh Do for technical support of the PCB and construction of the test configurations.

Conflicts of Interest: The authors declare no conflict of interest.

Appendix A. Clarke and Park Transformation

Clarke transformation, retrieved from [34]

$$i_\alpha = \frac{2}{3}\left(i_\mathrm{a} - \frac{1}{2}(i_\mathrm{b} + i_\mathrm{c})\right) \tag{A1}$$

$$i_\beta = \frac{1}{\sqrt{3}}\left(i_\mathrm{b} - i_\mathrm{c}\right) \tag{A2}$$

Park transformation, retrieved from [35]:

$$i_\mathrm{d} = i_\beta sin(\theta_\mathrm{e}) + i_\alpha cos(\theta_\mathrm{e}) \tag{A3}$$

$$i_\mathrm{q} = i_\beta cos(\theta_\mathrm{e}) - i_\alpha sin(\theta_\mathrm{e}) \tag{A4}$$

Appendix B. BLDC Motor Model in the Rotating Reference Frame

As FOC is used to commutate the stator windings, a model for BLDC motors is needed in the rotating reference frame (dq-frame). The standard BLDC circuit in the stationary abc frame is shown in Figure A1, where n v_{an}, i_{a}, R, L M_{s} is the motor neutral point, phase A line-neutral voltage, phase A current, stator resistance and mutual inductance between phases, respectively. The concentrated stator winding results in three trapezoidal shaped back-EMF's (e_{a}, e_{b}, e_{c}). From the figure, the corresponding time-domain model in the abc stationary reference frame is established (retrieved from [36]):

$$\begin{bmatrix} v_{\mathrm{an}} \\ v_{\mathrm{bn}} \\ v_{\mathrm{cn}} \end{bmatrix} = \begin{bmatrix} R & 0 & 0 \\ 0 & R & 0 \\ 0 & 0 & R \end{bmatrix} \begin{bmatrix} i_{\mathrm{a}} \\ i_{\mathrm{b}} \\ i_{\mathrm{c}} \end{bmatrix} + \frac{d}{dt} \begin{bmatrix} L & M_{\mathrm{s}} & M_{\mathrm{s}} \\ M_{\mathrm{s}} & L & M_{\mathrm{s}} \\ M_{\mathrm{s}} & M_{\mathrm{s}} & L \end{bmatrix} \begin{bmatrix} i_{\mathrm{a}} \\ i_{\mathrm{b}} \\ i_{\mathrm{c}} \end{bmatrix} + \begin{bmatrix} e_{\mathrm{a}} \\ e_{\mathrm{b}} \\ e_{\mathrm{c}} \end{bmatrix} \tag{A5}$$

Using the Park transformation (A24) on (A5), the model is transformed into the stationary dq reference frame (as shown in [36]):

$$\begin{bmatrix} v_{\mathrm{d}} \\ v_{\mathrm{q}} \end{bmatrix} = \begin{bmatrix} R + pL & -\omega_{\mathrm{m}} L \\ \omega_{\mathrm{m}} L & R + pL \end{bmatrix} \begin{bmatrix} i_{\mathrm{d}} \\ i_{\mathrm{q}} \end{bmatrix} + \omega_{\mathrm{m}} \lambda_{\mathrm{m}} \begin{bmatrix} f_{\mathrm{d}}(\theta_{\mathrm{e}}) \\ f_{\mathrm{q}}(\theta_{\mathrm{e}}) \end{bmatrix} \tag{A6}$$

where p, ω_{m}, λ_{m}, θ_{e} and $f_{\mathrm{d}}(\theta_{\mathrm{e}})$ is the number of poles within the motor, rotational velocity of the rotor, peak value of the magnetic flux linkage, electrical angle and auxiliary function (corresponding with the direct current component) modeling the trapezoidal back-EMF waveforms in the dq reference frame, respectively. Using FOC three sinusoidal line-neutral voltages are injected to generate three corresponding sinusoidal currents. In contrast to the PMSM, three perfectly shaped sinusoidal currents do not produce completely smooth torque, as the produced torque within the BLDC is obtained:

$$T = \frac{3}{2} p (\lambda_{\mathrm{m}} f_{\mathrm{q}}(\theta_{\mathrm{e}}) i_{\mathrm{q}} + \lambda_{\mathrm{m}} f_{\mathrm{d}}(\theta_{\mathrm{e}}) i_{\mathrm{d}}) \tag{A7}$$

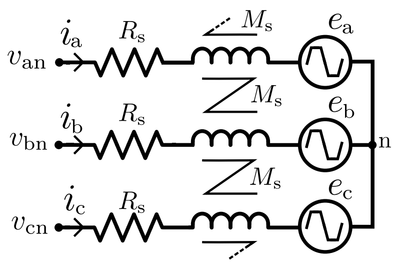

Figure A1. Schematic of the electrical components within the BLDC motor.

The problem is further addressed in [36–38], in which a modified Park method is proposed. This method uses an on-line estimation of the back-EMF harmonic contents and is used to calculate an angle and amplitude perturbation, which are injected into the phases. The injected currents counteract the effect of the trapezoidal back-EMF's, which results in smooth torque and higher efficiency. However, it requires extensive computation in the micro controller and the complexity increases. Instead, the motor is approximated as a PMSM, which greatly simplifies the modeling and control of the motor. This is simply done by setting $f_{\mathrm{d}} = 0$ and $f_{\mathrm{q}} = 1$:

$$\begin{bmatrix} v_{\mathrm{d}} \\ v_{\mathrm{q}} \end{bmatrix} \approx \begin{bmatrix} R + pL & -\omega_{\mathrm{m}} L \\ \omega_{\mathrm{m}} L & R + pL \end{bmatrix} \begin{bmatrix} i_{\mathrm{d}} \\ i_{\mathrm{q}} \end{bmatrix} + \omega_{\mathrm{m}} \lambda_{\mathrm{m}} \begin{bmatrix} 0 \\ 1 \end{bmatrix} \tag{A8}$$

It can be observed that i_{q} and i_{d} are coupled by $\pm\omega_{\mathrm{m}} L$ (also called the qd coupling terms) and are therefore interfering each other. Equation (A8) depicts the electrical model of the motor, which is sufficient for designing the torque and field controllers. For discrete observations of the motor states, the motor state-space model (without the qd and back-EMF coupling terms) can be estimated using Equation (A9).

$$A_\mathrm{k} = 1 - \frac{T_\mathrm{s} R}{L} \qquad B_\mathrm{k} = \frac{T_\mathrm{s}}{L} \qquad C = 1 \tag{A9}$$

where A_k, B_k is the discretized state transmission and input scalars, respectively, and C is the output scalar. As impedance control is required, the mechanical motor model is established from [39]:

$$\frac{d\omega_\mathrm{m}}{dt} = \frac{T_\mathrm{e} - T_\mathrm{l} - B\omega_\mathrm{m}}{J} \tag{A10}$$

where T_e, T_l, B and J is the electro-mechanical torque produced at the rotor shaft, load torque, friction damping constant and moment of inertia of the rotor, respectively. Assuming that the direct current component is zero ($i_\mathrm{d} \approx 0\,\mathrm{A}$):

$$T_\mathrm{e} \approx K_\mathrm{t} i_\mathrm{q} \tag{A11}$$

where K_t is the motor torque constant and can be calculated: $K_\mathrm{t} = \frac{3}{2} p \lambda_\mathrm{m}$. A mechanical and electrical motor transfer function (without the decoupling terms) is established by performing the laplace transformation of Equations (A8), (A10) and (A11) and solving for $\frac{\text{output}}{\text{input}}$:

$$G_\mathrm{elec}(s) = \frac{i_\mathrm{dq}(s)}{v_\mathrm{dq}(s)} = \frac{1}{L \cdot s + R} \tag{A12}$$

$$G_\mathrm{mech} = \frac{\omega_\mathrm{m}(s)}{T_\mathrm{e}(s)} = \frac{1}{J \cdot s + B} \tag{A13}$$

Similarly, the entire motor model (without the coupling terms), including both the electrical and mechanical transfer functions, becomes:

$$G_\mathrm{motor} = \frac{\omega_\mathrm{m}(s)}{v_\mathrm{q}(s)} = \frac{\lambda_\mathrm{m}}{(L \cdot s + R)(J \cdot s + B) + \lambda_\mathrm{m} K_\mathrm{t}} \tag{A14}$$

The provided models are based on parameters usually stated in the data sheet of the motor.

Appendix C. Controller Pseudo Algorithm

Using the error signals, $e_\mathrm{q}(k) = i_\mathrm{q}(k)^* - i_\mathrm{q}(k)$, $e_\mathrm{d}(k) = i_\mathrm{q}(k)^* - i_\mathrm{q}(k)$, the digital PI controllers calculate the quadrature and direct voltage components, by:

$$v_\mathrm{q}(k)^* = \overbrace{K_\mathrm{P} e_\mathrm{q}(k)}^{\text{proportional term}} \overbrace{+ K_\mathrm{I} \sum \frac{e_\mathrm{q}(k) + e_\mathrm{q}(k-1)}{2} T_\mathrm{s}}^{\text{integral term}} + \overbrace{\omega_\mathrm{m}(\lambda_\mathrm{m} + L i_\mathrm{d}(k))}^{\text{decoupling term}} \tag{A15}$$

$$v_\mathrm{d}(k)^* = \overbrace{K_\mathrm{P} e_\mathrm{d}(k)}^{\text{proportional term}} \overbrace{+ K_\mathrm{I} \sum \frac{e_\mathrm{d}(k) + e_\mathrm{d}(k-1)}{2} T_\mathrm{s}}^{\text{integral term}} - \overbrace{\omega_\mathrm{m} L i_\mathrm{q}(k)}^{\text{decoupling term}} \tag{A16}$$

Appendix D. Specifications of the Test Configuration

Table A1. Specifications of the U10PLUS KV80 motor and the controllers.

Description	Reference	Unit	Value
Internal Line Resistance	R	mΩ	95
Internal Line Inductance	L	µH	63.7
Max Continuous Current @180 s	I_{max}	A	33
Max Continuous Power @180 s	P_{max}	kW	1.5
Nominal Excitation Voltage	V_{DC}	V	40
Peak Stall Torque	T_{max}	N m	3.6
Max Operating Temperature	$T_{C,max}$	°C	180
Dimensions	DxT	mm	Ø89×40
Shaft Diameter	D_{shaft}	mm	15
Weight	M	g	500
Torque Constant	K_t	$\frac{Nm}{A}$	0.12
Velocity Constant	K_v	$\frac{RPM}{V}$	80
Number of poles	P	–	40
Moment of inertia on rotor	I	kg m^2	0.000 21
Motor viscous damping	B	$\frac{Nm}{rad/s}$	0.000 348
Torque controller proportional gain	K_p	$\frac{V}{Nm}$	0.5806
Torque controller integrator gain	K_i	$\frac{V}{Nms}$	819.5635
Speed controller proportional gain	$K_{p,\omega}$	$\frac{Nm}{rad/s}$	0.545
Speed/Angle observer gain	l		1500
Luenberger observer gain	L_k		0.4
Sampling/PWM period	Ts	µs	40
Magnetic encoder resolution	-	bits	12

Appendix E. Impedance Test Parameters

Table A2. Impedance model and controller parameters.

#	Impedance Model Parameters		Impedance Controller Parameters		
	Spring Constant K_s $\left[\frac{Nm}{rad}\right]$	Damping Constant B_s $\left[\frac{Nm}{rad/s}\right]$	Proportional Gain $K_{p,\Omega}$ $\left[\frac{Nm}{rad}\right]$	Derivative Gain $K_{d,\Omega}$ $\left[\frac{Nm}{rad/s}\right]$	Attenuation Factor α
Test 1	0.1	0.0029	0.8382	0.0255	0.0125
Test 2	1	0.0029	8.3822	0.002 55	0.1247
Test 3	2	0.0029	16.7645	0.0013	0.2495
Test 4	3	0.0029	25.1467	0.000 85	0.3742
Test 5	2	0.0029	16.7645	0.0013	0.2495
Test 6	2	0.0097	16.7645	0.0047	0.0681
Test 7	2	0.0193	16.7645	0.0095	0.0336
Test 8	2	0.0290	16.7645	0.0143	0.0222

Appendix F. Impact Test Parameters

Table A3. Impedance model and controller parameters.

#	Impedance Model Parameters		Impedance Controller Parameters	
	Spring Constant K_s $\left[\frac{Nm}{rad}\right]$	Damping Constant B_s $\left[\frac{Nm}{rad/s}\right]$	Proportional Gain $K_{p,\Omega}$ $\left[\frac{Nm}{rad}\right]$	Derivative Gain $K_{d,\Omega}$ $\left[\frac{Nm}{rad/s}\right]$
Test 1	0.1	0.029	0.0029	0.0029

Appendix G. Derivation of Torque and Field Controller Design Equations

Assuming relatively low rotational speed and high-bandwidth (or the back-EMF decoupling term is applied), the electrical transfer function becomes (A12):

$$G_{\text{motor,dq}}(s) = G_{\text{elec}}(s) = \frac{1}{L \cdot s + R} \tag{A17}$$

The transfer function of a PI controller in serial form is:

$$G_{\text{PI}}(s) = K_{\text{P}} \frac{\tau_{\text{I}} \cdot s + 1}{\tau_{\text{I}} \cdot s} \tag{A18}$$

where τ_{I} is the integrator time constant. This transfer function allows for a straight forward parameter design approach using the frequency domain method, called the Nyquist method. To be able to design the parameters using the bandwidth and phase margin, the transformation $s = j\omega$, (where j is the complex operator and ω is the rotational frequency) is used, along with the following rules, to calculate phase and magnitude of complex numbers:

$$z(\omega) = x(\omega) + jy(\omega) \qquad |Z|(\omega) = \sqrt{x(\omega)^2 + y(\omega)^2} \qquad \angle z(\omega) = \tan^{-1}\left(\frac{y(\omega)}{x(\omega)}\right) \tag{A19}$$

where $z(\omega)$ is a complex number consisting of the real part $x(\omega)$ and the imaginary part $y(\omega)$. Multiplying with a Zero-Order-Hold (ZOH) and applying z-transformation and, $G_{\text{ZOH}}(s)$, the electrical motor model (A12) is transformed into the discrete time domain:

$$\begin{aligned} G_{\text{elec}}(z) &= \mathscr{Z}\left\{G_{\text{ZOH}}(s)G_{\text{elec}}(s)\right\} = \frac{z-1}{z}\mathscr{Z}\left\{\frac{G_{\text{elec}}(s)}{s}\right\} = \frac{z-1}{z} \cdot \frac{1}{L} \cdot \frac{z(1-e^{-\frac{R}{L}T_{\text{s}}})}{\frac{R}{L}(z-1)(z-e^{-\frac{R}{L}T_{\text{s}}})} \\ &= \frac{1}{R} \cdot \frac{1-e^{-\frac{R}{L}T_{\text{s}}}}{z-e^{-\frac{R}{L}T_{\text{s}}}} \end{aligned} \tag{A20}$$

Now, the open-loop transfer function (without the PI controller) is multiplied with the PWM delay $G_{\text{PWM,delay}}(s) = e^{-s \cdot T_{\text{s}}}$ and transformed back into the s-domain, using bilinear transformation, as it maps the discrete time poles and zeros into the s-domain, making it possible to apply the Nyquist method:

$$\frac{i_{\text{dq}}}{v_{\text{dq}}}(s) \approx G_{\text{PWM,delay}}(s)G_{\text{elec}}(z)\bigg|_{z=\frac{1+s\frac{T_{\text{s}}}{2}}{1-s\frac{T_{\text{s}}}{2}}} = \frac{1}{R}\frac{1-e^{-\frac{R}{L}T_{\text{s}}}}{\frac{1+s\frac{T_{\text{s}}}{2}}{1-s\frac{T_{\text{s}}}{2}} - e^{-\frac{R}{L}T_{\text{s}}}} e^{-s \cdot T_{\text{s}}} \tag{A21}$$

$$= \frac{1-e^{-\frac{R}{L}T_{\text{s}}}}{R} \cdot \frac{(1-s\frac{T_{\text{s}}}{2})}{s\frac{T_{\text{s}}}{2}(1+e^{-\frac{R}{L}T_{\text{s}}}) + (1-e^{-\frac{R}{L}T_{\text{s}}})} e^{-s \cdot T_{\text{s}}} \tag{A22}$$

Multiplying with the transfer function of the integrator term gives the open-loop transfer function (without the proportional gain), which corresponds with the field and torque loops in Figure 3:

$$\frac{G_{\text{OL,dq}}(s)}{K_{\text{P}}} = G_{\text{I}}(s)\frac{i_{\text{dq}}}{v_{\text{dq}}}(s) = \frac{\tau_{\text{I}}s+1}{\tau_{\text{I}}s} \cdot \frac{1-e^{-\frac{R}{L}T_{\text{s}}}}{R} \cdot \frac{1-s\frac{T_{\text{s}}}{2}}{s\frac{T_{\text{s}}}{2}(1+e^{-\frac{R}{L}T_{\text{s}}}) + (1-e^{-\frac{R}{L}T_{\text{s}}})} e^{-s \cdot T_{\text{s}}} \tag{A23}$$

Using pole-zero cancellation ($\tau_{\text{I}} = \tau_{\text{elec}} = \frac{L}{R}$) result in constant 90° phase shift and a linear decaying magnitude (in the frequency spectrum) with $-20\,\text{dB}$ (if sample delay is not included). This means that the bandwidth of the integrator is as high as possible without adding extra phase shift at higher frequencies. This is highly beneficial as, by closing the loop, the system becomes a purely first order system (including sample delay), which makes it possible to design a highly robust controller.

In addition, it makes the motor controller sample and PWM delay the only limiting factor regarding closed-loop controller bandwidth, which is essential for achieving a high controller bandwidth. Using Equation (A19), the desired controller crossover frequency ω_c is calculated by aiming a phase margin of 60°:

$$\begin{aligned}60^\circ =&\pi + \tan^{-1}\left(\frac{\tau_I}{1}\right) - \tan^{-1}\left(\frac{\tau_I \cdot \omega_c^*}{0}\right) + \tan^{-1}\left(\frac{-\omega_c^* \frac{T_s}{2}}{1}\right) - \tan^{-1}\left(\frac{\omega_c^* \frac{T_s}{2}(1+e^{-\frac{R}{L}T_s})}{1-e^{-\frac{R}{L}T_s}}\right)\\ &- \tan^{-1}\left(\frac{\sin(\omega_c^* T_s)}{\cos(\omega_c^* T_s)}\right)\end{aligned} \tag{A24}$$

The resulting open-loop gain at the desired controller crossover frequency, without the proportional gain, is calculated:

$$\begin{aligned}\frac{|G_{OL,dq}(\omega_c^*)|}{K_P} =& \frac{\sqrt{(\tau_I\omega_c^*)^2+1^2}}{\sqrt{(\tau_I\omega_c^*)^2}} \cdot \frac{1-e^{-\frac{R}{L}T_s}}{R} \cdot \frac{\sqrt{(-\omega_c^* \frac{T_s}{2})^2+1^2}}{\sqrt{(\frac{T_2}{2}\omega_c^*(1+e^{-\frac{R}{L}T_s}))^2+(1-e^{-\frac{R}{L}T_s})^2}}\\ &\cdot \sqrt{\cos(T_s\omega_c^*)^2+\sin(T_s\omega_c^*)^2}\end{aligned} \tag{A25}$$

The proportional gain is now determined by: $K_P = \left(\frac{|G_{OL,dq}(\omega_c^*)|}{K_P}\right)^{-1}$ as it results in crossing 0 dB at the desired controller crossover frequency. As the digital PI controllers (shown in Appendix C) are at parallel form, the conversion: $K_I = \frac{K_P}{\tau_I}$ is done. The calculated K_P and K_I are the upper boundaries for the controller bandwidth that satisfy a phase margin of exactly 60°.

Appendix H. Symbolic Expressions of the Sensitivity Factors

The sensitivity factors are calculated assuming a stationary condition, where the true angle θ is constant 0 rad.

Appendix H.1. Direct and Quadrature Current with Respect to Measured Angle

$$S^{i_q}_{\Delta\theta_e}(\bar{\Delta}\theta_e, I_a, I_b, I_c) = \frac{\sqrt{3}\cos(\bar{\Delta}\theta_e)\left(\frac{I_b}{2} - \frac{I_c}{2}\right)}{3} - \sin(\bar{\Delta}\theta_e)\left(\frac{2I_a}{3} + \frac{I_b}{6} + \frac{I_c}{6}\right) \tag{A26}$$

$$S^{i_d}_{\Delta\theta_e}(\bar{\Delta}\theta_e, I_a, I_b, I_c) = \frac{\sqrt{3}\sin(\bar{\Delta}\theta_e)\left(\frac{I_b}{2} - \frac{I_c}{2}\right)}{3} + \cos(\bar{\Delta}\theta_e)\left(\frac{2I_a}{3} + \frac{I_b}{6} + \frac{I_c}{6}\right) \tag{A27}$$

Assuming a balanced system ($I_{abc} = I_A = I_B = I_C$) and that the angle encoder noise is zero-mean, the sensitivities become:

$$S^{i_q}_{\Delta\theta_e}(\bar{\Delta}\theta_e, I_{abc}) = -\sin(\bar{\Delta}\theta_e)I_{abc} \approx 0 \tag{A28}$$

$$S^{i_d}_{\Delta\theta_e}(\bar{\Delta}\theta_e, I_{abc}) = \cos(\bar{\Delta}\theta_e)I_{abc} \approx I_{abc} \tag{A29}$$

Appendix H.2. Direct and Quadrature Current with Respect to Measured Currents

It makes no sense to derive the sensitivity factors of the direct and quadrature currents (i_q, i_d) with respect to each phase current (i_a, i_b, i_c), since they change with respect to the electrical angle θ_e. Hence, combined sensitivity factors are derived instead, which assumes that three similar current sensors (equal mean and variance) are used and that they are stochastically independent:

$$S^{i_q}_{\Delta i_{abc}} = \sqrt{\left(S^q_a\right)^2 + \left(S^q_b\right)^2 + \left(S^q_c\right)^2} \tag{A30}$$

$$S^{i_d}_{\Delta i_{abc}} = \sqrt{\left(S^{d}_{a}\right)^2 + \left(S^{d}_{b}\right)^2 + \left(S^{d}_{c}\right)^2} \tag{A31}$$

By substituting (A36), (A37) and (A38) into (A1) and (A2) and substituting them into (A3) and (A4) and afterwards applying (A40) to both formulas, the sensitivity of the quadrature and direct currents with respect to each phase currents are derived. Assuming zero-mean angle sensor noise, the combined phase current sensitivities become:

$$\begin{aligned} S^{i_q}_{\Delta i_{abc}}(\bar{\Delta\theta}_e) &= \sqrt{\left(\frac{2\cos(\bar{\Delta\theta}_e)}{3}\right)^2 + \left(\frac{\cos(\bar{\Delta\theta}_e)}{3} - \frac{\sqrt{3}\sin(\bar{\Delta\theta}_e)}{3}\right)^2 + \left(\frac{\cos(\bar{\Delta\theta}_e)}{3} + \frac{\sqrt{3}\sin(\bar{\Delta\theta}_e)}{3}\right)^2} \\ &\approx \sqrt{\left(\frac{2}{3}\right)^2 + \left(\frac{1}{3}\right)^2 + \left(\frac{1}{3}\right)^2} = 0.8165 \end{aligned} \tag{A32}$$

$$\begin{aligned} S^{i_d}_{\Delta i_{abc}}(\bar{\Delta\theta}_e) &= \sqrt{\frac{4\sin(\bar{\Delta\theta}_e)^2}{9} + \left(\frac{\sin(\bar{\Delta\theta}_e)}{3} - \frac{\sqrt{3}\cos(\bar{\Delta\theta}_e)}{3}\right)^2 + \left(\frac{\sin(\bar{\Delta\theta}_e)}{3} + \frac{\sqrt{3}\cos(\bar{\Delta\theta}_e)}{3}\right)^2} \\ &\approx \sqrt{0 + \left(-\frac{\sqrt{3}}{3}\right)^2 + \left(\frac{\sqrt{3}}{3}\right)^2} = 0.8165 \end{aligned} \tag{A33}$$

This suggests that both the quadrature and direct currents are highly affected by noise from the current sensors.

Appendix I. Field Oriented Control

This section describes the standard and well-known commutation strategy, referenced FOC. FOC is a commutation strategy that uses measured phase currents and rotor angle to calculate the current components, i_q and i_d. i_q is directly proportional to the torque generated at the rotor shaft and i_d is directly proportional to the field generated across the stator windings. This is feasible by using the Clarke and Park transformations and their corresponding mathematical inverses. As a Brushless Direct Current (BLDC) motor has a fixed field in the permanent magnets, there is no need to generate another field in the stator windings. Therefore, this method allows for high efficiency by enabling the possibility to force the field component (i_d) down to zero. In addition, high bandwidth torque control is possible by using PID controllers. The process of the conversion is illustrated in Figure A2.

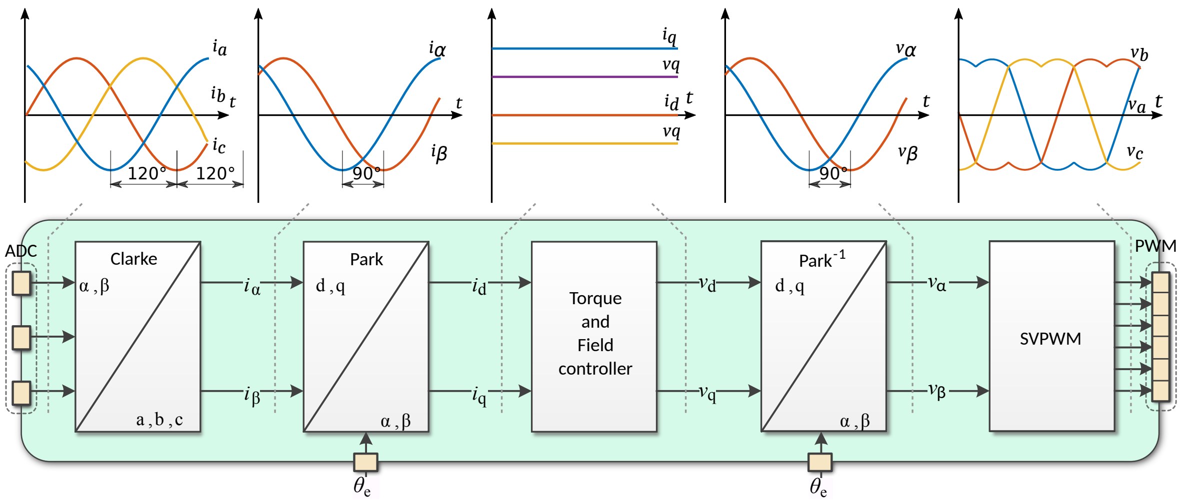

Figure A2. Illustration of the FOC commutation strategy and resulting waveforms. The turquoise box outlines the Digital Signal Processor (DSP) tasks used in FOC.

Using the Clarke transformation, three measured phase currents (i_a, i_b and i_c) are converted from three rotating currents, equal in amplitude and shifted by 120° (assuming a balanced system), to two rotating currents (i_α and i_β) shifted by 90°. Transformation Equations (A1) and (A2) are available in Appendix A.

The Park transformation is used to convert the two rotating currents (i_α and i_β) to two stationary current components (i_q and i_d) using Equations (A3) and (A4) in Appendix A. The two current components (i_q, i_d), that are stationary components in the rotating reference frame, can be controlled using PID controllers which generate the quadrature and direct voltages (v_q, v_d). Inverse park is used to convert the voltages into the rotating reference frame (v_α, v_β) by applying the mathematical inverse of Equations (A3) and (A4) in Appendix A. Space Vector Pulse Width Modulation or another modulation technique may now be applied to generate the six corresponding Pulse Width Modulated (PWM) signals that drive the six MOSFETs in a three-phase inverter.

Appendix J. Noise Analysis Based on the Sensitivity Method

The standard and well-known sensitivity method [40,41] is applied to the motor model to analyze the noise in the system and thereby quantify the impact of each sensor's noise. This facilitates the study of how much sensor uncertainties impact the quadrature current and the direct current feedbacks. This is an important study as it sheds light on how to reduce noise in the system.

The quadrature i_q and direct current i_d equations, with respect to the sensor inputs, are determined by substituting (A1) and (A2) into (A3) and (A4) (Appendix A):

$$i_q(i_a, i_b, i_c, \theta_e) = \frac{2}{3}\left(i_a - \frac{1}{2}(i_b + i_c)\right)\cos(\theta_e) - \frac{1}{\sqrt{3}}\left(i_b - i_c\right)\sin(\theta_e) \tag{A34}$$

$$i_d(i_a, i_b, i_c, \theta_e) = \frac{2}{3}\left(i_a - \frac{1}{2}(i_b + i_c)\right)\sin(\theta_e) + \frac{1}{\sqrt{3}}\left(i_b - i_c\right)\cos(\theta_e) \tag{A35}$$

The phase currents are assumed to be sinusoidal (as FOC is applied). In addition, the motor phases are assumed to be balanced meaning that the phase currents are zero-mean, equal in amplitude and are 120° out of phase with respect to each other. All sensor noise is assumed to be zero-mean additive. Hence:

$$i_a = I\sin(\theta + \theta_{qd}) + \Delta i_a \tag{A36}$$

$$i_b = I\sin(\theta + 120^\circ + \theta_{qd}) + \Delta i_b \tag{A37}$$

$$i_c = I\sin(\theta + 240^\circ + \theta_{qd}) + \Delta i_c \tag{A38}$$

$$\theta_e = \theta + \Delta\theta_e \tag{A39}$$

The first terms are the true currents and angle and the last terms are the absolute sensor and interface errors. θ and θ_{qd} are the true angle and the angle of the qd current vector sum $\vec{i}_{qd} = \vec{i}_d + \vec{i}_q$ (in the qd rotating reference frame), respectively. θ_{qd} is typically 90° as that corresponds to the rotor being aligned with the q-axis (which is desired to produce maximum torque). The goal is to determine how sensitive the direct and quadrature currents are to the sensor uncertainties, $(\Delta i_a, \Delta i_b, \Delta i_c, \Delta\theta)$. Each sensitivity factor is calculated at true angles, $\theta = 0\,\text{rad}$, by substituting (A36), (A37), (A38) and (A39) into (A34) and (A35) and afterwards applying (A40) to them.

$$S_x^R = \frac{\partial R}{\partial x} \tag{A40}$$

where S_x^R is the absolute sensitivity of the output R with respect to the input x. The sensitivity factors are further derived in Appendix H. The results suggest that the quadrature current (or the produced torque) is immune to infinitesimally small angle noise (as $S_{\Delta\theta_e}^{i_q} \approx 0$) while it is highly affected by noise from the current sensors (as $S_{\Delta i_{abc}}^{i_q} \approx 0.8165$). Additionally, the direct current (or the produced field) is highly affected by both currents and angle sensor noise (as $S^{i_d}_{\Delta i_{abc}} \approx 0.8165$ and $S^{i_d}_{\Delta i_{abc}} \approx I_{abc}$). However, by deploying the i_q and i_d feedbacks in a closed-loop system including PI controllers (as shown in Figure 2), the sensor uncertainties are filtered by an amount determined by the design of the PI controllers. The PI controllers are typically low-pass filters meaning that a low controller bandwidth will filter the sensor noise accordingly. As high-bandwidth control is required, the filtering effect will be small and another approach to filter the direct and quadrature currents is therefore needed. As current sensor noise highly effects both currents these must be filtered to enable high-bandwidth, low-noise motor control. However, it is even more important to filter the angle measurements based on the following reasons:

- High-end and off-the-shelf magnetic encoders are typically maximum 12-bit resolution
- The direct current is highly affected by angle sensor noise
- The Proportional-Derivative (PD) controller amplifies angle sensor noise which is almost directly injected into the motor phases (due to high-bandwidth torque control)
- If speed feed-forward is required (to decouple the torque loop from the back-EMF), the angle sensor value is once again amplified and injected directly into the motor phases

Appendix K. Impact Force Benchmark Test Configuration

To properly test an actuator before deploying it in a compliant robot, a load that is able to produce load conditions similar to worst case conditions in the specific application is required. For many compliant robotics systems, the worst case scenario (in terms of controller stability and power transfer) is during impacts as this requires a huge amount of force to be mitigated in a fast and controlled manner. This scenario generates lots of stress on the mechanics as well as electronics while it forces the motor controller software loops to be operated under non-linear saturated conditions. Therefore, a simple linear load configuration is proposed that mimics impact force similar to dropping a legged robot from a specific distance or a collision between an industrial or collaborative robot and an external element. The entire test configuration is illustrated in Figure A3.

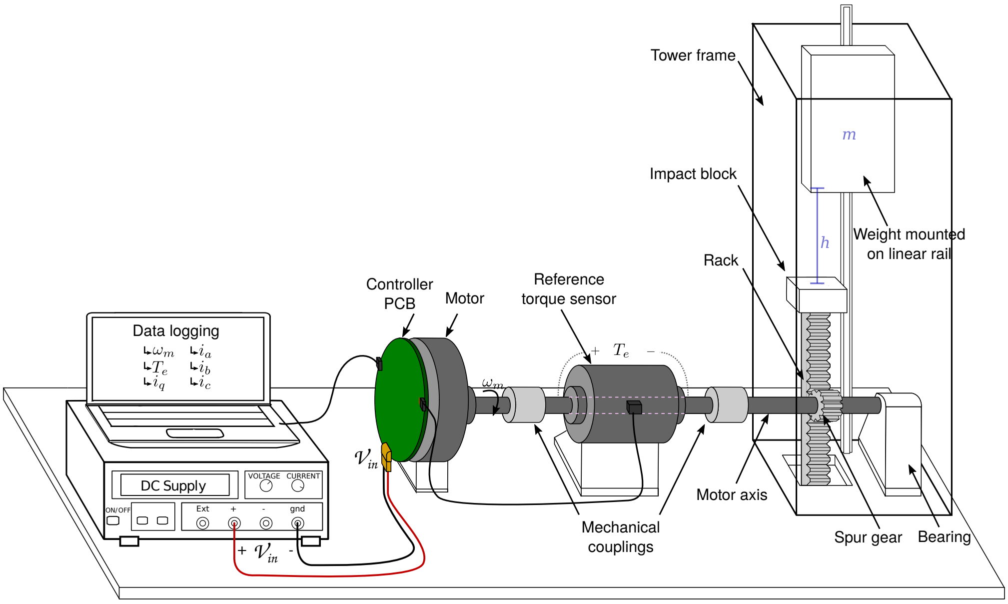

Figure A3. Illustration of the test configuration used for testing the motor controller during impact forces.

The actuator design in this situation is a Direct-Drive (DD) Brushless Direct Current (BLDC) motor. To be able to measure the rotational torque, a reference torque sensor may be deployed between the motor and the linear load. The linear load consists of a spur gear which drives the rack up and down. The impact force is generated by releasing the mass m from a certain distance down to the impact block h. Before doing so, the motor controller is programmed to fix the impact block at a specific distance. The mass m and the height h should be determined to reflect the worst case impact force that may occur for the specific compliant robotic application. However, the gear ratio acquired between the spur gear and rack should be taken into account.

Appendix L. Electronics and Software Platform

A superficial overview of the electronics and software platform used for this project is illustrated in Figure A4.

The Texas Instruments (TI) TMS320F28069 Digital Signal Processor (DSP) is a 32-bit platform which includes two 90 MHz processors that can communicate with each other and with a great variety of peripherals using the memory bus. The platform and its modules, libraries, peripherals and processors are all optimized for motor control which facilitates a simple, fast and optimized implementation. All three control loops depicted in Figure 3 (Field, Impedance and Torque loops), as well as the PWM signals, are running at 25 kHz. The programmable TI DRV8323SRTAR chip is used for current measurements amplification and gate drives. Three of the dual transistors, CSD88599Q5DC, are used in the three-phase inverter to deliver the power to the motor. Three LTSR 15-NP current sensors are used as they include highly linear and low noise capabilities. The programmable 12-bit angular magnetic encoder Integrated Circuit (IC), AM4096Q, from RLS is deployed as it enables high precision and resolution angle sensing and as it includes incremental output which is easily interfaced with the DSP (using the eQEP module). The entire motor module, mounted on a test stand, is illustrated in Figure A5. As shown, the Printed Circuit Board (PCB) is designed such that it is compact and fits behind the motor which results in short sensor and phase leads, decreasing propagation delay and loss. Phase correct PWM is used and interrupt is enabled which triggers the motor controller loop when the counter compare register reaches the highest counter value. At that time, all switching-related oscillations are settled, thus current sensor noise is reduced in relation to using interrupts on the rising-edge of one of the PWM signals. In addition, the mean current within the switching period is measured which is in agreement with the motor models applied in the observers and controller designs.

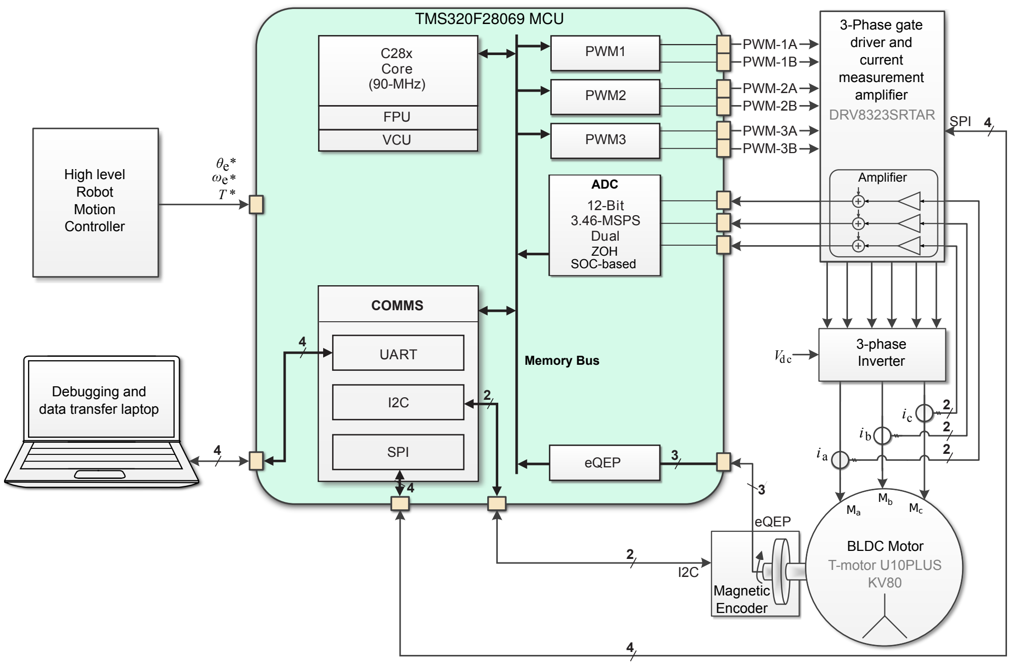

Figure A4. Illustration of all relevant communication between the TMS320F28069 DSP and the external components which are utilized in the motor controller PCB (manufactured at University of Southern Denmark (SDU)).

Note that all embedded motor controller project files as well as PCB project and gerber files are available as supplementary materials ("C code S13" and "PCB files S14").

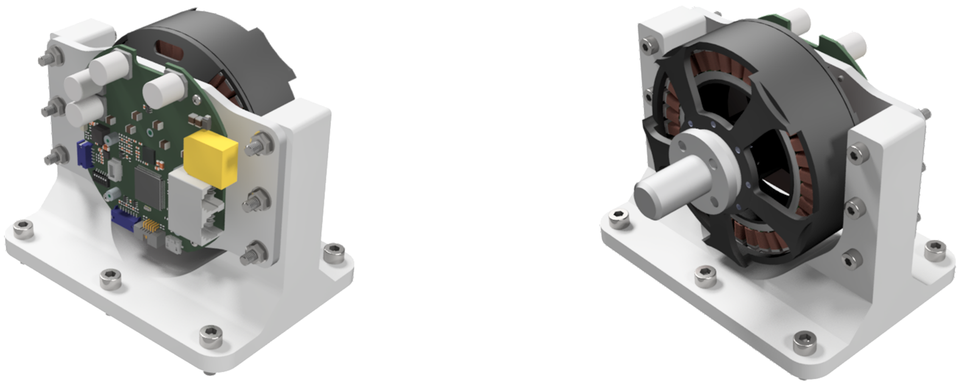

(**a**) (**b**)

Figure A5. Rendered 3D models of the entire motor module hardware, including (**a**) the U10 PLUS KV80 motor and (**b**) the motor controller PCB developed at SDU. The motor module is mounted on the 3D print model test stand.

References

1. Wensing, P.M.; Wang, A.; Seok, S.; Otten, D.; Lang, J.; Kim, S. Proprioceptive actuator design in the MIT cheetah: Impact mitigation and high-bandwidth physical interaction for dynamic legged robots. *IEEE Trans. Robot.* **2017**, *33*, 509–522. [CrossRef]
2. Vallery, H.; Veneman, J.; van Asseldonk, E.; Ekkelenkamp, R.; Buss, M.; van Der Kooij, H. Compliant actuation of rehabilitation robots. *IEEE Robot. Autom. Mag.* **2008**, *15*, 60–69. [CrossRef]
3. Androwis, G.J.; Nolan, K.J. Evaluation of a Robotic Exoskeleton for Gait Training in Acute Stroke: A Case Study. In *Wearable Robotics: Challenges and Trends*; Springer: Cham, Switzerland, 2017; Volume 16, pp. 9–13. [CrossRef]
4. Sharifi, M.; Salarieh, H.; Behzadipour, S.; Tavakoli, M. Biomedical Signal Processing and Control Beating-heart robotic surgery using bilateral impedance control: Theory and experiments. *Biomed. Signal Process. Control* **2018**, *45*, 256–266. [CrossRef]
5. Williams, M.R.; Andrea, S.D.; Herr, H.M. Impact on gait biomechanics of using an active variable impedance prosthetic knee. *J. NeuroEng. Rehabil.* **2016**, *13*, 54. [CrossRef]
6. Milwich, M.; Selvarayan, S.K.; Gresser, G.T. Fibrous materials and textiles for soft robotics. In *Soft Robotics: Transferring Theory to Application*; Springer: Berlin, Germany, 2015; p. 11. [CrossRef]
7. Gracia, L.; Perez-vidal, C.; Valls-miro, J. Advanced Mathematical Methods for Collaborative Robotics. *Math. Probl. Eng.* **2018**, *2018*, 10–13. [CrossRef]
8. Beltran-Carbajal, F.; Valderrabano-Gonzalez, A.; Favela-Contreras, A.; Hernandez-Avila, J.L.; Lopez-Garcia, I.; Tapia-Olvera, R. An Active Vehicle Suspension Control Approach with Electromagnetic and Hydraulic Actuators. *Actuators* **2019**, *8*, 35. [CrossRef]
9. Vanderborght, B.; Albu-schaeffer, A.; Bicchi, A.; Burdet, E.; Caldwell, D.G. Variable impedance actuators: A review. *Robot. Autonomous Syst.* **2013**, *61*, 1601–1614. [CrossRef]
10. Boaventura, T.; Medrano-Cerda, G.A.; Semini, C.; Buchli, J.; Caldwell, D.G. Stability and performance of the compliance controller of the quadruped robot HyQ. In Proceedings of the IEEE International Conference on Intelligent Robots and Systems, Tokyo, Japan, 3–7 November 2013; pp. 1458–1464. [CrossRef]
11. Roozing, W.; Malzahn, J.; Kashiri, N.; Caldwell, D.G.; Tsagarakis, N.G. On the Stiffness Selection for Torque-Controlled Series-Elastic Actuators. *IEEE Robot. Autom. Lett.* **2017**, *2*, 2255–2262. [CrossRef]
12. Katz, B.G. A Low Cost Modular Actuator for Dynamic Robots. Master's Thesis, Massachusetts Institute of Technology, Cambridge, MA, USA, 2018.
13. Bhatia, A.; Johnson, A.M.; Mason, M.T. Direct Drive Hands: Force-Motion Transparency in Gripper Design. In Proceedings of the Robotics: Science and Systems, Freiburg, Germany, 22–26 June 2019.

14. Verstraten, T.; Beckerle, P.; Furnémont, R.; Mathijssen, G. Series and Parallel Elastic Actuation: Impact of natural dynamics on power and energy consumption. *MAMT* **2016**, *102*, 232–246. [CrossRef]
15. Hogan, N. Impedance Control: An Approach to Manipulation. In Proceedings of the 1984 American Control Conference, San Diego, CA, USA, 6–8 June 1984; pp. 304–313. [CrossRef]
16. Semini, C.; Barasuol, V.; Boaventura, T.; Frigerio, M.; Focchi, M.; Caldwell, D.G.; Buchli, J. Towards versatile legged robots through active impedance control. *Int. J. Robot. Res.* **2015**, *34*, 1003–1020. [CrossRef]
17. Gabriel, R.; Leonhard, W.; Nordby, C.J. Field-Oriented Control of a Standard AC Motor Using Microprocessors. *IEEE Trans. Ind. Appl.* **1980**, *IA-16*, 186–192. [CrossRef]
18. Schindlbeck, C.; Haddadin, S. Unified Passivity-Based Cartesian Force/Impedance Control for Rigid and Flexible Joint Robots via Task-Energy Tanks. In Proceedings of the 2015 IEEE International Conference on Robotics and Automation (ICRA), Seattle, WA, USA, 26–30 May 2015; pp. 440–447. [CrossRef]
19. Niccol, L.R.; Molinari, L. Discrete-Time Formulation for Optimal Impact Control in Interaction Tasks. *J. Intell. Robot. Syst.* **2018**, *90*, 407–417.
20. Cherubini, A.; Passama, R.; Crosnier, A.; Lasnier, A.; Fraisse, P. Robotics and Computer-Integrated Manufacturing Collaborative manufacturing with physical human—Robot interaction. *Robot. Comput. Integr. Manuf.* **2016**, *40*, 1–13. [CrossRef]
21. Roveda, L. A User-Intention Based Adaptive Manual Guidance with Force-Tracking Capabilities Applied to Walk-Through Programming for Industrial Robots. In Proceedings of the 2018 15th International Conference on Ubiquitous Robots (UR), Honolulu, HI, USA, 26–30 June 2018; pp. 369–376. [CrossRef]
22. Roveda, L. Adaptive Interaction Controller for Compliant Robot Base Applications. *IEEE Access* **2019**, *7*, 6553–6561. [CrossRef]
23. Kim, S.H. Sensorless technique using the motor model. In *Electric Motor Control: DC, AC, and BLDC Motors*; Elsevier Science: Amsterdam, The Netherlands, 2017.
24. Kshirsagar, P.; Burgos, R.P.; Jang, J.; Lidozzi, A.; Wang, F.; Boroyevich, D.; Sul, S.K. Implementation and sensorless vector-control design and tuning strategy for SMPM machines in fan-type applications. *IEEE Trans. Ind. Appl.* **2012**, *48*, 2402–2413. [CrossRef]
25. Chi, S.; Zhang, Z.; Xu, L. Sliding-mode sensorless control of direct-drive PM synchronous motors for washing machine applications. *IEEE Trans. Ind. Appl.* **2009**, *45*, 582–590. [CrossRef]
26. Kim, S.H. Vector Control of Permanent Magnet Synchronous Motors. In *Electric Motor Control: DC, AC, and BLDC Motors*; Chapter 5.5; Elsevier Science: Amsterdam, The Netherlands, 2017.
27. Mon-Nzongo, D.L.; Jin, T.; Ekemb, G.; Bitjoka, L. Decoupling Network of Field-Oriented Control in Variable-Frequency Drives. *IEEE Trans. Ind. Electron.* **2017**, *64*, 5746–5750. [CrossRef]
28. Hyun, D.J.; Seok, S.; Lee, J.; Kim, S. High speed trot-running: Implementation of a hierarchical controller using proprioceptive impedance control on the MIT Cheetah. *Int. J. Robot. Res.* **2014**, *33*, 1417–1445. [CrossRef]
29. Luenberger, D. Introduction To Observers. *IEEE Trans. Autom. Control* **1971**, *AC16*, 596–602. [CrossRef]
30. Kalman, R.E. A New Approach to Linear Filtering and Prediction Problems. *J. Basic Eng.* **2011**, *82*, 35. [CrossRef]
31. Horváth, Z.; Molnárka, G. Design Luenberger Observer for an Electromechanical Actuator. *Acta Technica Jaurinensis* **2014**, *7*, 328–343. [CrossRef]
32. Alessandri, A.; Coletta, P. Design of Luenberger Observers for a Class of Hybrid Linear Systems. In Proceedings of the International Workshop on Hybrid Systems: Computation and Control (HSCC 2001), Rome, Italy, 28–30 March 2001; pp. 7–18. [CrossRef]
33. Li, M.; Kang, R.; Branson, D.T.; Dai, J.S. Model-Free Control for Continuum Robots Based on an Adaptive Kalman Filter. *IEEE/ASME Trans. Mechatron.* **2018**, *23*, 286–297. [CrossRef]
34. Schulz, M.W.; Clarke, E. Determination of Instantaneous Currents and Voltages by Means of Alpha, Beta, and Zero Components. *Trans. Am. Inst. Electr. Eng.* **1951**, *70*, 1248–1255.
35. Park, R.H. Two Reaction Theory of Synchronous Machines Generalized Method of Analysis-Part I. *Trans. Am. Inst. Electr. Eng.* **1929**, *48*, 716–727. [CrossRef]
36. Lazor, M.; Stulrajter, M. Modified field oriented control for smooth torque operation of a BLDC motor. In Proceedings of the 10th International Conference, ELEKTRO 2014, Žilina, Slovakia, 19–20 May 2014; pp. 180–185. [CrossRef]

37. Kshirsagar, P.; Krishnan, R. High-efficiency current excitation strategy for variable-speed nonsinusoidal back-EMF PMSM machines. *IEEE Trans. Ind. Appl.* **2012**, *48*, 1875–1889. [CrossRef]
38. Oliveira, A.A.; De Monteiro, J.R.; Aguiar, M.L.; Gonzaga, D.P. Extended DQ transformation for vectorial control applications of non-sinusoidal permanent magnet synchronous machines. In Proceedings of the PESC Record—2005 IEEE 36th Power Electronics Specialists Conference, Recife, Brazil, 16 June 2005; pp. 1807–1812. [CrossRef]
39. Kumar, M.; Singh, B.; Singh, B.P. Modeling and Simulation of Permanent Magnet Brushless Motor Drives using Simulink. In Proceedings of the National Power Systems Conference, Kharagpur, India, 27–29 December 2002; Volume 1, pp. 253–258, .
40. Saltelli, A. Sensitivity Analysis for Importance Assessment—Risk Analysis. *Risk Anal.* **2002**, *22*, 579–590. [CrossRef]
41. Saltelli, A.; Ratto, M.; Andres, T.; Campolongo, F.; Cariboni, J.; Gatelli, D.; Saisana, M.; Tarantola, S. *Methods and Settings for Sensitivity Analysis—An Introduction*; Global Sensitivity Analysis—The Primer, John Wiley & Sons, Ltd.: Chichester, UK, 2002; Chapter 1.2, Volume 52.